



저작자표시-비영리-변경금지 2.0 대한민국

이용자는 아래의 조건을 따르는 경우에 한하여 자유롭게

- 이 저작물을 복제, 배포, 전송, 전시, 공연 및 방송할 수 있습니다.

다음과 같은 조건을 따라야 합니다:



저작자표시. 귀하는 원저작자를 표시하여야 합니다.



비영리. 귀하는 이 저작물을 영리 목적으로 이용할 수 없습니다.



변경금지. 귀하는 이 저작물을 개작, 변형 또는 가공할 수 없습니다.

- 귀하는, 이 저작물의 재이용이나 배포의 경우, 이 저작물에 적용된 이용허락조건을 명확하게 나타내어야 합니다.
- 저작권자로부터 별도의 허가를 받으면 이러한 조건들은 적용되지 않습니다.

저작권법에 따른 이용자의 권리는 위의 내용에 의하여 영향을 받지 않습니다.

이것은 [이용허락규약\(Legal Code\)](#)을 이해하기 쉽게 요약한 것입니다.

[Disclaimer](#)

Master of Science

고온 산업 응용을 위하여 알루미늄 기판에  
증착된 ZnO/Pt 나노아일랜드의 매우 안정적인  
수소감지 특성

Highly stable hydrogen sensing properties of the  
ZnO/Pt nanoisland deposited on alumina substrate for  
high temperature industrial applications

The Graduate School  
of the University of Ulsan  
School of Electrical, Electronic and Computer Engineering

Md Mayen Uddin

**Highly stable hydrogen sensing properties of the  
ZnO/Pt nanoisland deposited on alumina substrate  
for high temperature operated industrial applications**

Supervisor: Prof. Hyeon Cheol Kim

A Dissertation

Submitted to  
the Graduate School of the University of Ulsan  
in partial fulfillment of the requirements  
for the degree of

Master of Science

by

Md Mayen Uddin

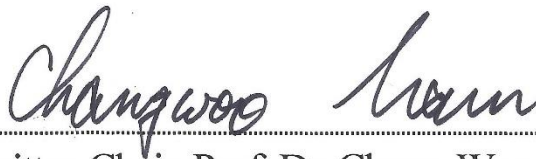
School of Electrical, Electronic and Computer Engineering

Ulsan, Republic of Korea

August 2021

**Highly stable hydrogen sensing properties of the  
ZnO/Pt nanoisland deposited on alumina substrate  
for high temperature operated industrial applications**

This certifies that the Master's Thesis  
of Md Mayen Uddin is approved.



.....  
Committee Chair, Prof. Dr. Chang-Woo Nam



.....  
Committee Member, Prof. Dr. Hyeon Cheol Kim



.....  
Committee Member, Prof. Dr. Tae-woo Kim

Department of Electrical, Electronic and Computer Engineering

Ulsan, Republic of Korea

August 2021

## **ACKNOWLEDGEMENT**

All praise and thanks belong to almighty ALLAH (SWT).

I would like to express my sincere gratitude to my advisors Prof. Dr. Hyeon Cheol Kim of the School of Electrical Engineering at University of Ulsan for his supervisions, advice, continuous support, and constant encouragement throughout my M.Sc. study and related research. His patience, motivation, immense knowledge, and continuous guidance helped me in all the time of research and writing of this thesis. Besides my advisors, I am gratefully indebted to my thesis committee: Prof. Dr. Hyeon-Cheol Kim, Prof. Dr. Chang-Woo Nam, Prof. Dr. Tae-Woo Kim, for their efforts to go through my thesis, insightful comments, and encouragement, which incited me to widen my research from various perspectives.

I am very much grateful to University of Ulsan for giving me such a wonderful research environment and financial support. This university gave me the chance to conduct several useful courses with excellent instructors that will give me a way to think and work properly in the rest of my life. I would like to express my hearties thanks to university and research center's staffs for their help and support. My special thanks go to Brain Korea 21Plus Program for its contribution and financial support during my study.

I would like to thank my fellow lab mates Mr. Shovon Talukder, Mr. Junhee Lee and Mr. Forhaz Farid in Smart Microsystem Laboratory for their friendship and support. I am grateful to Mr. Habibur Rahaman and Mohammad Rashedul Hasan for enlightening me the first glance of research.

I am ever grateful to my mother Monjuma Begum and father Mohammad Ali for raising me and helping me to achieve all that I have in my life. Last but not the least, I would like to thank my brothers, especially Amir Walid, Atish Bhattacharjee, Rafia Nishat Toma, Md Nazim Uddin, Md Junayed Hasan and Nasim Al Islam as well as extended family members, and close friends for their love, support and understanding.

University of Ulsan

August 13, 2021

Md Mayen Uddin

## ABSTRACT

In this work, the Pt decorated ZnO nanoparticles layers are deposited on alumina substrate using the magnetron sputtering method (RF sputtering) and then analyzed with rapid detection of hydrogen gas for an extremely stable hydrogen detecting characteristics. AFM, XRD, and contact angle analysis were utilized to examine the impacts of the rapid thermal annealing (RTA) process at high temperatures. In comparison to the as-grown ZnO film, the XRD spectra of the samples after RTA treatment shows a significant improvement in the amplitude and a shrinking of the (002) diffraction peak's full width at half-maximum (FWHM). FE-SEM and XPS were used to characterize samples to determine the best material structure for stable sensing performance. In terms of higher operating temperature (300°C), stronger selectivity, and long-term durability are obtained from the ZnO-Pt system, which exhibited the best dynamic and transient gas sensing behaviors. The optimum sensor had a detection range of 100-1000 ppm, with response rates of 4.2 percent and 14.9 percent for 100 and 1000 ppm, respectively. More importantly, the sensor shows highly stable base resistance ( $\sim 132.5\Omega$ ) and sensing response ( $\sim 14.9\%$ ) for a long-term period of the test. Sensitivity to 1000 ppm NO, CH<sub>4</sub>, CO, C<sub>3</sub>H<sub>8</sub>, and O<sub>2</sub> gas was only -0.2%, -0.16%, 0.6%, 0.15%, and 0.4% respectively, showing excellent selectivity. In conclusion, the obtained ZnO/Pt nanoparticles layers on alumina substrate are indeed a worthy material for building high temperature working environments where high-performance H<sub>2</sub> gas sensors are needed.

# TABLE OF CONTENTS

Acknowledgement.....	i
Abstract.....	iii
Table of contents.....	iv
List of figures.....	vi
List of tables.....	viii
<b>CHAPTER 1 Introduction</b>	
1.1 Motivation.....	2
1.2 Objectives.....	3
1.3 Thesis organization.....	4
<b>CHAPTER 2 Literature review and background</b>	
2.1 Overview of the highly stable hydrogen sensor's importance.....	8
2.2 Specifications for stable hydrogen sensors.....	10
2.3 Types of hydrogen sensor .....	11
2.4 Hydrogen analysis using nanomaterials.....	13
2.4.1 Platinum's (Pt) advantages in hydrogen gas sensing.....	14
2.4.2 Catalytic Pt based on hydrogenation and dehydrogenation motivation.....	14
2.5 Summary.....	16
<b>CHAPTER 3 Experimental procedures and evaluation</b>	
3.1 Substrate selection .....	18
3.2 Optimization of ZnO nanoparticles .....	21
3.3 ZnO nanoparticles development.....	24
3.4 Pt metal deposition at ZnO nanoparticles .....	25
3.5 Electrodes (Au) deposition .....	26
3.6 The device fabrication process .....	27
3.7 Evaluation methods for Pt@ZnO stable gas sensor .....	28
3.7.1 Atomic force microscopy .....	29
3.7.2 FESEM (Field emission scanning electron microscopy) .....	30



3.7.3	X-ray diffraction analysis (XRD).....	30
3.7.4	Water contact angle system .....	30
3.7.5	X-ray photoelectron spectroscopy (XPS).....	31
3.7.6	EDS elemental analysis and mapping .....	31
3.7.7	Measuring gas sensing properties .....	31
3.8	Summary.....	32
<b>CHAPTER 4 Stable hydrogenation and dehydrogenation performance analysis of Pt@ZnO nanoislands decorated over alumina</b>		
4.1	Structural, morphological, and compositional characteristics .....	34
4.2	Gas sensing properties of ZnO/Pt NPs .....	46
4.3	Summary.....	55
<b>CHAPTER 5 Conclusions and future work</b>		
5.1	Conclusions.....	58
5.2	Future work suggestions .....	59
List of publications by the author.....		60
References .....		61
Appendix .....		67

## LIST OF FIGURES

<b>Figure 2.1</b>	Hydrogen sensor applications.....	10
<b>Figure 2.2</b>	Applications for detecting hydrogen .....	11
<b>Figure 2.3</b>	Hydrogen sensor state of art.....	16
<b>Figure 3.1</b>	Optical images of alumina substrate .....	19
<b>Figure 3.2</b>	(a) Optical image of ZnO target (b) Distance between the substrate and target.....	19
<b>Figure 3.3</b>	RF magnetron sputtering system.....	21
<b>Figure 3.4</b>	Measurement of surface conductivity .....	22
<b>Figure 3.5</b>	Water contact angle of optimum ZnO on alumina.....	23
<b>Figure 3.6</b>	Rapid thermal annealing system .....	24
<b>Figure 3.7</b>	Pt target (iTASCO, 99.99% purity) .....	26
<b>Figure 3.8</b>	(a) Au target (b) Optical image of the as prepared device .....	27
<b>Figure 3.9</b>	(a, b) Device fabrication process of ZnO-Pt hydrogen sensor .....	28
<b>Figure 3.10</b>	Hydrogenation and dehydrogenation measuring setup .....	32
<b>Figure 4.1</b>	AFM analysis of ZnO nanoparticles (a) as-grown; (b) 800°C; (c) 900°C; (d) 1000°C; and (e) 1100°C, respectively.....	34
<b>Figure 4.2</b>	FE-SEM surface analysis for sample (S0-S4); (1a-5a) Surface morphologies of ZnO-Pt (inset higher magnification images) and (1b-5b) radius distribution for each sample.....	37
<b>Figure 4.3</b>	XRD analysis of (a) as-grown and annealed at 800°C; 900°C; 1000°C; 1100°C; ZnO NPs respectively (b) ZnO-Pt nanoparticles before and after annealing.....	39

<b>Figure 4.4</b>	Contact angle analysis of ZnO nanoparticles; (a, b) as grown; (c, d) 800°C; (e, f) 900°C; (g, h) 1000°C; (i, j) 1100°C and (k, l) sample S3; for diiodomethane and water, respectively.....	41
<b>Figure 4.5</b>	XPS analysis for the sample S0 (1a, 1b, 1c); S1 (2a, 2b, 2c); S2 (3a, 3b, 3c); S3 (4a, 4b, 4c); S4 (5a, 5b, 5c), respectively.....	45
<b>Figure 4.6</b>	EDS (a) elemental (b) mapping analysis for S3 sample .....	46
<b>Figure 4.7</b>	Schematic setup of high temperature (300°C) hydrogen sensor testing.....	48
<b>Figure 4.8</b>	Response-recovery time and stabilize sensor performance analysis of the samples S0-S4 (a-e) at 1000 ppm at high temperature (300°C) hydrogen gas.....	50
<b>Figure 4.9</b>	Transient response characteristics of S3 (200-400-600-800-1000 ppm) at 300°C working temperature.....	52
<b>Figure 4.10</b>	Long term stability of the S3 sensor in case of (a) base resistance and (b) response, exposed to 1000 ppm H <sub>2</sub> gas at 300°C working temperature.....	53
<b>Figure 4.11</b>	Sensor linear correlation according to the Langmuir model.....	55
<b>Figure 4.12</b>	Sample S3 selectivity histogram for different test gases.....	56

## LIST OF TABLES

<b>Table 2.1</b>	Different types of hydrogen sensor's .....	12
<b>Table 3.1</b>	Operating conditions of RF magnetron sputtering for ZnO target....	20
<b>Table 3.2</b>	ZnO nanoparticle size optimization by RF magnetron system.....	22
<b>Table 3.3</b>	Water contact angle and surface energies of ZnO nanoparticles.....	23
<b>Table 3.4</b>	Pt nanoparticle deposition conditions .....	25
<b>Table 3.5</b>	Au nanoparticle deposition conditions.....	26
<b>Table 3.6</b>	Evaluation methods .....	29
<b>Table 4.1</b>	AFM Measurements for ZnO nanoparticles at different annealing conditions.....	35
<b>Table 4.2</b>	XRD analysis of 002 peak of ZnO NPs prepared at different annealing conditions.....	40
<b>Table 4.3</b>	Calculation of contact angle and surface energy for various annealing surfaces of ZnO nanoparticles.....	43
<b>Table 4.4</b>	Study of XPS measurements for sample S0~S4.....	44

# CHAPTER 1

---

## Introduction

The purpose of this chapter is to provide a general framework and introduction for the work presented in this Master thesis. This chapter is divided into three sections, addressing the research motivations, objectives, and thesis organization.

## **1.1 Motivation**

Hydrogen ( $H_2$ ) is a colorless, odorless, and tasteless gas that, when blended with air, can pose a safety danger due to its wide flammability spectrum (4~75%), which raises the likelihood of high burning rates and explosive tendencies. It may also function as an asphyxiant at elevated concentrations.  $H_2$  is used as a reactant in the chemical industry to treat ammonia, petrochemicals, and methanol. It is also used as a source of electricity, with notable uses in fuel cell and rocket propulsion systems. The creation of a hydrogen economy fueled by sunlight is becoming more feasible, with renewed focus on the processing of  $H_2$  by photo catalytic water splitting. Furthermore,  $H_2$  extracted from renewable sources of sustainable energy can be used as a feedstock for catalytic hydrogenation reactions that turn  $CO_2$  into a usable fuel, which not only provides fuels with a higher energy density than  $H_2$ , but also absorbs a harmful greenhouse gas. If such an energy system is to develop, it would need to be tracked by a network of sensors that can detect  $H_2$  levels where it is used, delivered, and processed. If dispersed  $H_2$  power generation systems become commonplace in this scenario, such point-of-use consumption can eventually render  $H_2$  sensors as important as carbon monoxide and smoke detectors.

## 1.2 Objectives

This study reports the stability of nanoscale platinum (Pt) decorated ZnO nanoparticles formed on a rough alumina substrate was investigated. Ultra-high vacuum RF magnetron sputtering was used to deposit thin ZnO films, which were then subjected to a phase of rapid annealing process to induce the arrangement of NPs morphological and crystalline structures. To shape a sensing film, Pt was deposited on the ZnO nanoparticles using RF magnetron sputtering. The structure of nanomaterials ZnO particles allows for greater adsorption integration with the catalyst metal, Pt. Furthermore, the particle configuration is intended to have a permeated conductive pathway by increasing the supply of Pt metal at the nanometer scale and the structure that is exceptionally stable for high-temperature hydrogen sensors. The objectives of this work are illustrated below:

- Stable hydrogenation and dehydrogenation properties
- Good sensitivity
- Wider detection range
- Linearity in large detection range (100 to 1000 ppm)
- Good repeatability in 1000 ppm
- Elevated temperature (300°C)
- Light weight, small size
- Highly hydrophobic catalytic substrate.

For evaluating the hydrogenation and dehydrogenation properties, we optimized the ZnO nanoislands structure and grew different nano sized ZnO particles by varying the deposition conditions and applied rapid thermal annealing process to connect the particles by coalescence mechanism. After coalescence, these modified nanostructured particles revealed islands structure, which later helped to use a percolated islands structure with improved ohmic conduction. The nanostructure of Pt metal to be deposited for hydrogen permeation and deportation was greatly aided by this percolating channel. Pt metal with a high surface-to-volume ratio was then deposited on top of the ZnO nanoislands. Finally, we investigated hydrogenation and dehydrogenation in a practical gas field by adding a bias voltage, which resulted in rapid reaction and recovery, as well as improvements in hydrogen stability.

### **1.3 Thesis organization**

The aim of this study is to show how the author's analysis was presented both theoretically and experimentally. The fabrications, theoretical investigation, and characterization of Pt coated at ZnO nanoparticles over alumina substrate as a hydrogenation and dehydrogenation model were all examined in depth. Furthermore, evaluating the hydrogenation and dehydrogenation of the as-prepared model expands the capabilities of a stable hydrogen sensor for use in safety applications, allowing for greater sensitivity and selectivity. The thesis is organized as follows:



- **Chapter 1.** Introduction

A short introduction and motivation behind the study, and overall works contents are illustrated in this section.

- **Chapter 2.** Literature review and background

Backgrounds of this study along with nanomaterials familiarization and the state of the art are discussed elaborately in this section.

- **Chapter 3.** Experimental procedures and evolution

All experiments steps and device fabrications processes along with experimental tools and their processes were explained elaborately in this section.

- **Chapter 4.** Hydrogenation and dehydrogenation performance analysis of

Pt@ZnO nanoislands decorated over alumina.

- **Chapter 5.** Conclusions and future work

The overall outcomes of this research are summarized in this section. Furthermore, some suggestions for the improvement of this model were also analyzed for the future work related to this research are discussed.

## CHAPTER 2

---

### Literature review and background

Background and the necessity of this research, working mechanism, performance enhancing relative factors, and the state of the art relative to this research have been discussed in this chapter.

## **2.1 Overview of the highly stable hydrogen sensor's importance**

It is well known that hydrogen ( $H_2$ ) is the most optimistic, pristine, and efficient combustible sources of energy due to its many advantages such as high calorific value of combustion, quick ignition time, and significant potential for future applications. However, as the  $H_2$  is colorless and odorless gas, it can explosive and flammable at a low concentration of 4% in the atmosphere [1–3]. Therefore, reliable gas sensors are highly desirable for applications in high temperature areas ( $\geq 300^\circ C$ ) such as metal productions, renewable energy supplies, fuel cells, space shuttle propulsion, environmental, agricultural, industries, etc. to detect the  $H_2$  leakage due to their harmfulness and the associated threat to the ecosystem. Hence, the detecting framework in need is relied upon to be a sensor combination with multidisciplinary detecting advancements. The high-temperature gas sensor is exceptionally wanted to screen the harmful gases at the higher working temperature ( $\geq 300^\circ C$ ). The gas detecting component can be dictated by 3S factors (i.e., selectivity, sensitivity, and stability). All things considered, a couple of sensors are accounted for to show an adequate 3S execution for genuine natural application [4–6]. While a large portion of the gas sensors are accounted for to work at moderate working temperature ( $< 300^\circ C$ ) [3,7,8]. Due to the contradictory definition of high temperature and technological difficulties in the past, only a few studies have been found to present higher operating temperature gas output

( $\geq 300^\circ\text{C}$ ), despite the growing interest in harsh environment gas sensing due to the urgent need from industrial or nuclear power stations. Furthermore, the majority of the high temperature experiments were carried out in a laboratory setting [4].

Recently, various catalytic metal oxide semiconductor sensors such as  $\text{TiO}_2$  [9–11],  $\text{SnO}_2$  [2,12–14],  $\text{WO}_3$  [15–18],  $\text{ZnO}$  [19–23] and CNT [24] are investigated for their ability to detect hydrogen gas with strong working stability, high precision, and a quick manufacturing procedure. Among them,  $\text{ZnO}$  has unique characteristics and broad application expectations due to its wide and coordinate band gap of  $3.37\text{eV}$  along with a significant amount of exciton binding energy ( $60\text{ meV}$ ) and an oxygenated surface [21,25,26]. Also,  $\text{ZnO}$  has a broad range of utilizations in sensors, thin film semiconductors, LEDs, and sun-oriented cells [27–29], etc. It is commonly utilized as a gas detection substance because of its superior permeable electrical conductivity as well as outstanding mechanical stability under sensor operating environment. Among numerous gas-delicate substance,  $\text{ZnO}$  has pulled in the consideration of numerous scientists because of its huge explicit surface zone and evident surface impacts. Furthermore, Sensors made of  $\text{ZnO}$  were broadly utilized in the investigation of an assortment of combustible gases and destructive gases. Apparently, there are not many examinations on high temperature  $\text{H}_2$  sensors with a high reaction dependent on materials made of pure  $\text{ZnO}$  [30].



**Fig 2.1.** Hydrogen sensor applications

## 2.2 Specifications for stable hydrogen sensors

- Safe performance i.e., sensor construction that is explosion proof, as well as a protective housing.
- Low power consumption with easy device integration, and a user friendly
- Sensitivity and precision at a higher degree of temperature (300°C)
- Stable signal with smooth response and recovery cycles without any noise
- High selectivity and low cross sensitivity
- Less hysteresis and high repeatability
- Small size, low expense, longer life span, and easy operation and maintenance

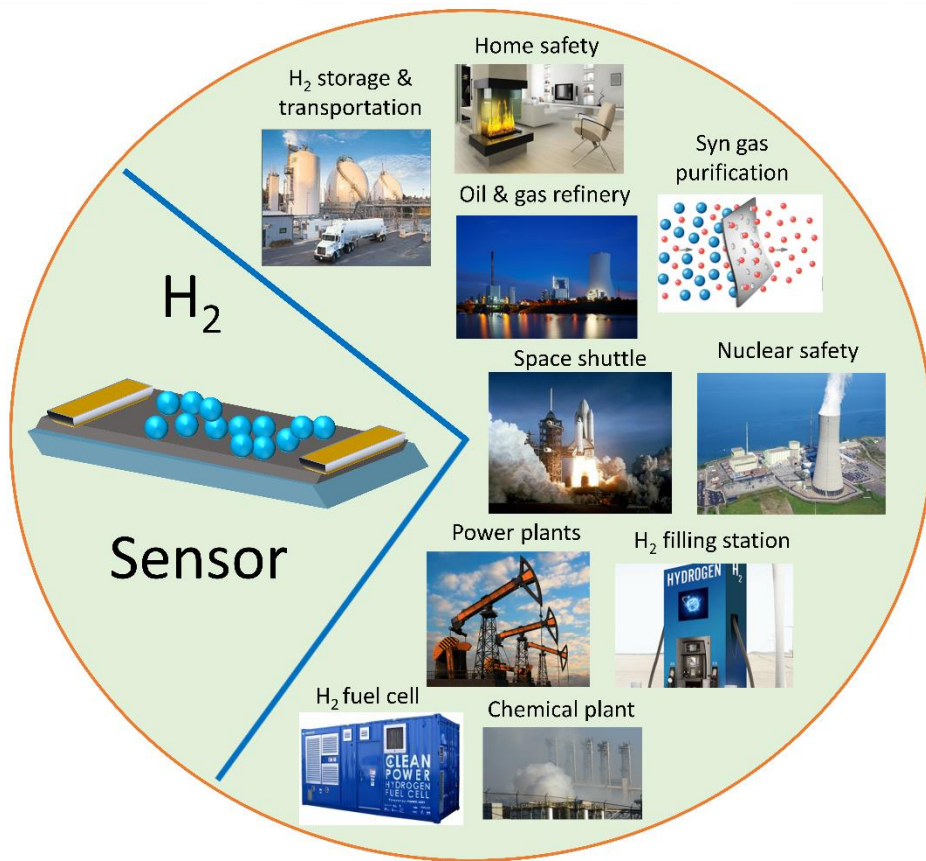


**Fig. 2.2.** Applications for detecting hydrogen

### 2.3 Types of hydrogen sensor

Hydrogen sensor have been widely researched for their wide range of uses in case of catalytic, thermal conduction, electro-chemical, resistive, optical, and acoustic etc. However, the resistive type sensor have been demonstrate well for its high sensitivity, fast response, low cost, and power consumption. **Table 2.1** summarizes the different type of hydrogen sensor.

**Table 2.1.** Different types of hydrogen sensor's

Sensor type	Operating principle	Physical change	Advantages	Disadvantages
Catalytic	Pellistor	Temperature Resistance	<ul style="list-style-type: none"> <li>-Long lifetime</li> <li>-Wide temperature &amp; pressure range</li> <li>-Stable output with aging</li> </ul>	<ul style="list-style-type: none"> <li>-Not selective for hydrogen</li> <li>-Poisoned by Si, P compounds &amp; S</li> <li>-High power consumption</li> <li>-Requires 5-10% O<sub>2</sub> to oxidation</li> </ul>
Thermal conduction	Thermal conductivity	Temperature Resistance	<ul style="list-style-type: none"> <li>-Wide detection range</li> <li>-Does not require O<sub>2</sub></li> <li>-Resistant to poisoning</li> <li>-Long life</li> </ul>	<ul style="list-style-type: none"> <li>-Can not detect less than 1 %</li> <li>-Reference gas needed</li> </ul>
Electro-chemical	Amerpometric	Diffusion limited current	<ul style="list-style-type: none"> <li>-Wide temperature range</li> <li>-Resistant to poisoning</li> <li>-Long life</li> </ul>	<ul style="list-style-type: none"> <li>-Less response time</li> <li>-Additional gas permeable membrane needed</li> </ul>
Resistive	Semiconducting metal oxide	Resistance	<ul style="list-style-type: none"> <li>-High sensitivity</li> <li>-Fast response</li> <li>-Good lifetime</li> <li>-Wide temperature range</li> <li>-Low cost</li> </ul>	<ul style="list-style-type: none"> <li>-Cross selectivity</li> <li>-Humidity influence</li> <li>-Contamination susceptible to aging</li> </ul>

Work function	Schottky diode(metal-semiconductor)  MOS field effect transistor	Current-voltage peculiarities	-Small size -Mass production -Fast response  -Highly sensitive and selective  -Small size	-High temperature operating needed high band gap based semiconductor.  -High power consumption  -Low detection limit
Optical	Optrodes	Changes in reflectivity	-Operate in absent of oxygen  -Wide detection range	-Slow response time  -Susceptible to poisoning
Acoustic	Surface acoustic wave	Frequency	-High sensitivity  -Room Temperature operation  -Wide detection range	-Unstable at higher temperature  -Humidity effect

## 2.4 Hydrogen analysis using nanomaterials

Nanomaterials have been widely researched for their wide range of uses in the pharmaceutical industry, medical fields, food technology, national security, and everyday life. Nanotechnology's exponential growth is propelling the world's technology to new heights. Complex nanomaterials research is used to create high-performance electronics and sensors. Metal oxide, cement materials, 2D materials, ceramic materials, and other nanomaterials are among them. Nanostructured catalytic metals and metal oxide semiconductor materials are among them, and their interactions



with various gases in the atmosphere are being researched extensively. The ease with which they could be manufactured and the intriguing nanoscale impact on their physical and chemical properties made them ideal for analysis and analysis. Since ZnO, SnO<sub>2</sub>, WO<sub>3</sub>, and TiO<sub>2</sub> have catalytic effects on hydrogen molecules, they need a higher power consumption (temperature greater than 300°C) to operate. Noble metals such as Pt, Pd, Au, Mg, Ni were used with metal oxides (ZnO, SnO<sub>2</sub>, WO<sub>3</sub>, TiO<sub>2</sub>) and carbon materials to boost hydrogenation and dehydrogenation reaction at an elevated temperature and comparatively lower power consumption.

#### **2.4.1 Platinum's (Pt) advantages in hydrogen gas sensing**

Platinum (Pt) has been widely analyzed and investigated as a high-sensitivity and selectivity hydrogen sensing material. Platinum has proved to be a reliable catalyst for a wide range of oxidation and reduction reactions in both acidic and basic electrolytes, making it an excellent choice for process feasibility tests. This next-generation catalyst is referred to as "HP," which stands for "High Power Catalysts." It is a fcc crystal structure-based metal with an atomic weight and number of 195.084 and 78 respectively and electronic configuration of [Xe] 4f<sup>14</sup>5d<sup>9</sup>6s<sup>1</sup> also its melting point is 1768°C. At the time of physical absorption in hydrogenation, hydrogen molecules selectively absorbed in the Pt surface (fcc) and dissociated on the interstitial sites of Pt.

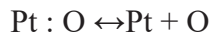
#### **2.4.2 Catalytic Pt based on hydrogenation and dehydrogenation motivation**

Two mechanisms could explain the observed rise in the response to H<sub>2</sub> in Pt-catalyzed ZnO films (Pt@ZnO NPs). One is based on oxygen spillover, and the other is

based on the regulation of the Fermi stage when Pt nanoparticles are present on the ZnO surface. Both contribute to accelerated oxygen chemisorption and dissociation:



The Pt:O complex thus formed is capable of dissociating to release oxygen singlets.



The labile oxygen atoms spillover from the Pt surface to the ZnO surface, creating additional  $\text{O}_2^-$  or  $\text{O}^{2-}$  ions through the pathways outlined above, and resulting in a high electrostatic potential near the contact point. Additionally, the work functions of Pt (~5.60 eV) and ZnO (~4.09 eV) show a significant contrast. The degradation zone at the surface of the metal oxides and the ZnO film surface grows because of this. As a result, more electrons are attracted from the ZnO conduction band onto the Pt surface, resulting in a greater number of active sites than on the pristine ZnO surface. As a result, when  $\text{H}_2$  molecules react with these adsorbed oxygen compounds, the width of the depletion zone and the height of the surface barrier change. As a result, the Pt@ZnO sensor is more involved than the one that is not decorated.

The state of the art for metal oxide based hydrogen sensor has been summarized in **Fig.**

### 2.3.

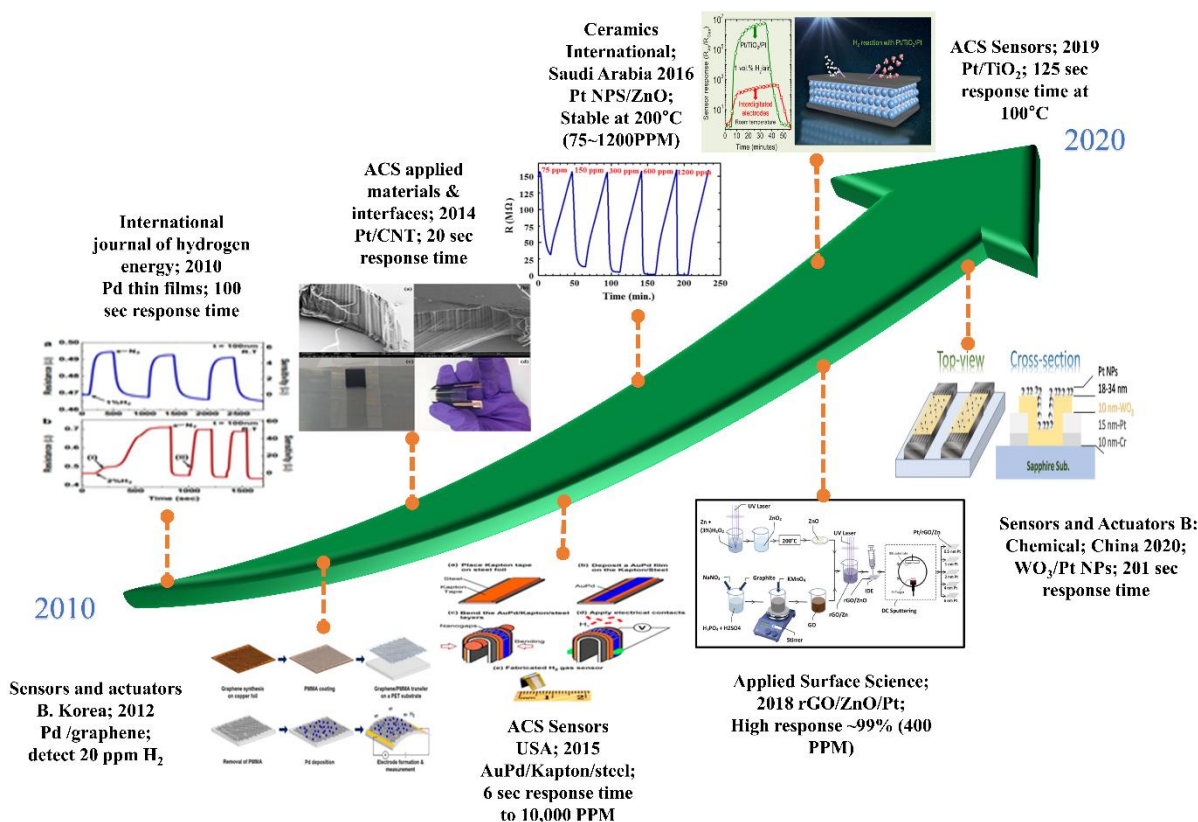


**Fig. 2.3.** Hydrogen sensor state of art

### 2.5 Summary

In conclusion, owing to their material and structural properties, metallic ZnO structures are preferred for safe hydrogen sensing, as shown by the literature review. Furthermore, by preparing a scarcity current direction between two electrodes on their respective surfaces, decorated Pt/ZnO metal on alumina substrates improved hydrogen sensing characteristics.

# CHAPTER 3

---

## Experimental procedures and evaluation

To develop ZnO nanoparticles on a highly rough alumina substrate, several experimental steps were carried out. The morphology of ZnO nanoparticles was crucial in improving the stable hydrogenation and dehydrogenation phenomena, as well as their reaction magnitude. Furthermore, it improved surface interaction at the nanoscale level by increasing the surface to volume ratio, which improved the synergetic effects of gas absorption and desorption. Despite the need for a high temperature of 300°C to completely dehydrogenate in 112 sec, a smooth hydrogenation period of 133 sec was measured for 1000 ppm hydrogen gas at 14.9% response magnitude.

ZnO nanoparticles were created by depositing an optimized sheet of ZnO thin film on an alumina substrate using an ultra-high vacuum radio frequency magnetron sputtering technique, then rapidly thermal annealing the layer to induce surface diffusion. Later, using the RF magnetron sputtering method, a Pt catalytic structure was also deposited.

### **3.1 Substrate selection**

The high roughness and hydrophobicity of commercially available alumina substrate is used to enhance the forming of nanostructured metal islands. First, an extremely rough alumina substrate (12×6 mm<sup>2</sup>) was washed for 5 minutes in ethanol, acetone, and isopropanol, then ultrasonicated for 15 minutes and dried with nitrogen gas, followed by heating in a hot plate at 100°C.

ZnO was sputtered on alumina substrate by RF magnetron sputtering before forming ZnO nanoparticles on it.

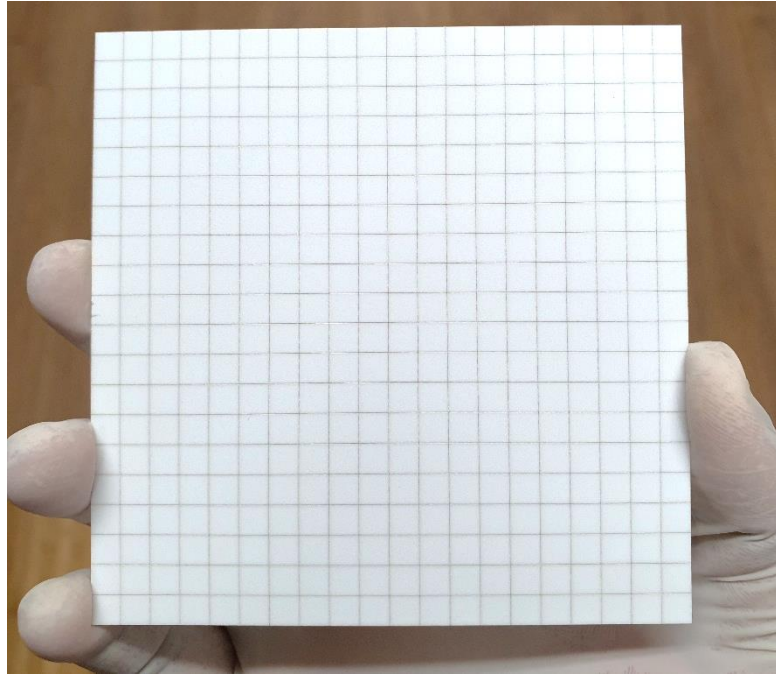


**Fig. 3.1.** Optical images of alumina substrate

By varying the RF magnetron sputtering deposition state, different sizes of ZnO nanoparticles were deposited. An extremely pure ZnO target (iTASCO, 99.99% purity) was used in the experiment, and a gap of 6cm was held between the substrate and the target in the sputtering chamber.

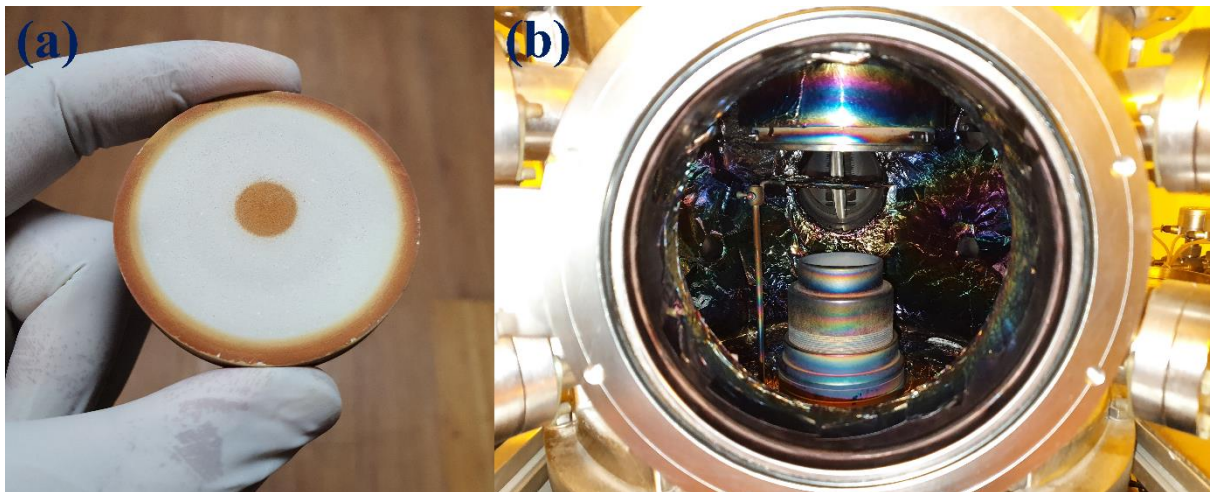


**Fig. 3.2.** (a) Optical image of ZnO target. (b) Distance between the substrate and target.

ZnO nanoparticles were deposited at a deposition pressure of 8 mTorr at a gas flow ratio of Ar:N<sub>2</sub> =1:10 after the sputtering chamber was evacuated with a pressure of 10 mTorr using a high vacuum rotary pump. The rate of deposition was nearly 0.19 nm/sec. The plasma was generated in the sputter chamber with a rf power of 100 W and vacuum conditions of (8 K). **Table 3.1** summarizes the parameters.

**Table 3.1.** Operating conditions of RF magnetron sputtering for ZnO target.

<b>Target</b>	ZnO (iTASCO, 99.99%)
<b>Target-substance distance</b>	6 cm
<b>Base pressure</b>	10 mTorr
<b>RF power</b>	100 watt
<b>Deposition pressure</b>	8 mTorr
<b>Deposition temperature</b>	8 Kelvin
<b>Deposition rate</b>	0.19 nm/sec



**Fig. 3.3.** RF magnetron sputtering system.

### **3.2 Optimization of ZnO nanoparticles**

Optimizing the ZnO nanoparticles morphology, which serves as a blueprint for increasing the nanoparticles/catalytic structure, is important for developing ZnO nanoparticles and deploying an interfacial catalytic layer for hydrogenation and dehydrogenation. A Keithely probe station system was used to check the surface conductivity for optimizing the ZnO morphology, as it is thought that a highly agglomerated and bulk size nanoparticle can bind together tightly and increase the surface conductivity. Furthermore, a bulk morphology of highly dense metal nanoparticles has a higher surface energy, which can impede nanoparticle growth by reducing surface diffusion.



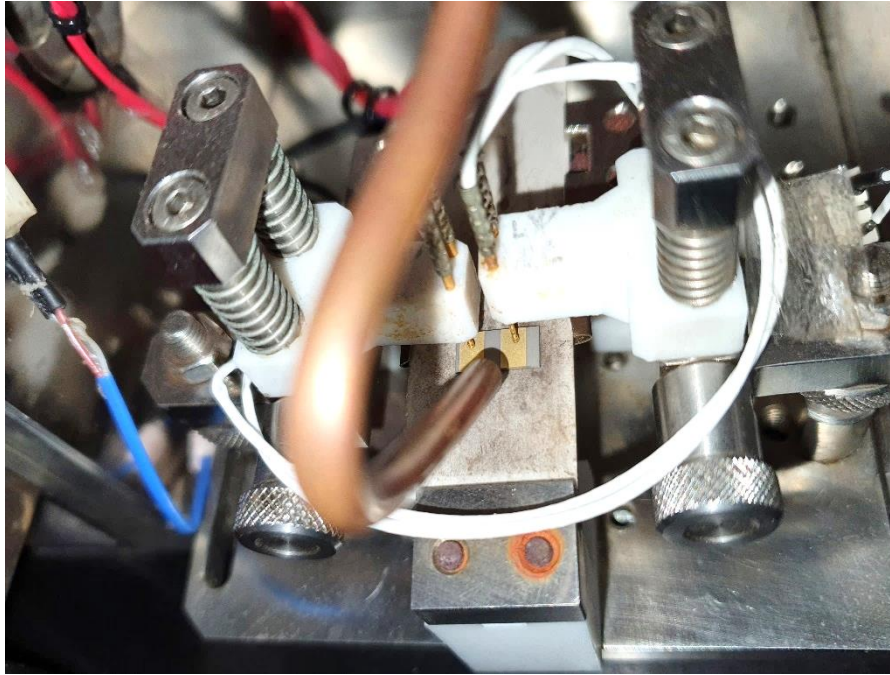


**Fig. 3.4.** Measurement of surface conductivity

As a result, various sizes of nanoparticles were deposited by adjusting the deposition time in RF magnetron sputtering to optimize the ZnO nanoparticle morphology. **Table 3.2** summarizes the circumstances and optimized scale performance.

**Table 3.2.** ZnO nanoparticle size optimization by RF magnetron system

Average nanoparticle size (nm)	Deposition time (min)	Surface resistivity ( $\Omega$ )
171	~ 15	~ $29.3 \times 10^3$
342	~ 30	~ $4.2 \times 10^3$
510	~ 45	~ 132.5

The water interface angle of ZnO nanoparticles on an alumina substrate was measured after they were deposited. For 510 nm ZnO nanoparticles deposited on an alumina substrate, a contact angle of 108.7° was found, as well as a solid vapor interfacial energy of 40.11 mN/m.



**Fig. 3.5.** Water contact angle of 510 nm ZnO on alumina

Because of the optimized surface energy between the nanoparticles and the substrate, this morphology provides an optimized surface resistivity of  $\sim 132.5 \Omega$ , which was enough to induce a thermal annealing diffusion process. The surface energy and water contact angle are summarized in **Table 3.3**.

**Table 3.3.** Water contact angle and surface energies of ZnO nanoparticles

Average nanoparticle size (nm)	Contact angle	Surface energy $\gamma_{SV}$ (mN/m)
171	87°	28.34 mN/m
342	98.5°	36.79 mN/m
510	108.7°	40.11 mN/m

### 3.3 ZnO nanoparticles development

A thermal annealing method was used to create the ZnO nanoislands after depositing and optimizing the ZnO nanoparticles on the alumina. A vacuum chamber was created using a vacuum pump. The annealing was done in an argon setting, with a mass flow controller feeding a 50 SCCM gas into the annealing chamber through a channel. The annealing method was set up in three stages. The temperature in the first or initial stage stays about 5 degrees Celsius, rising to 1000 degrees Celsius at a rate of 20 degrees Celsius per second in the second stage, where the time limit was set to 5 minutes. After that, a phase down process (third stage) was carried out at a slower rate of 5°C/sec.



**Fig. 3.6.** Rapid thermal annealing system

After the rapid thermal annealing process, all the samples were cooled down at room temperature for a post sputtering process.

### 3.4 Pt metal deposition at ZnO nanoparticles

For enhancing the hydrogenation and dehydrogenation catalytic phenomenon, Pt metal was deposited at ZnO nanoislands after the rapid thermal annealing process. Pt metal target of (99.99%) purity was deposited after ZnO deposition by varying the RF magnetron sputtering system's operating conditions. The conditions are given in **Table 3.4**.

**Table 3.4.** Pt nanoparticle deposition conditions

<b>Target</b>	<b>Pt (99.99%)</b>
<b>Target-substance distance</b>	8cm
<b>Base pressure</b>	10 mTorr
<b>RF power</b>	170 watt
<b>Deposition pressure</b>	8 mTorr
<b>Deposition temperature</b>	8 Kelvin
<b>Deposition rate</b>	1.42 nm /Sec



**Fig. 3.7.** Pt target (iTASCO, 99.99% purity)

### **3.5 Electrodes (Au) deposition**

After Pt metal deposition, Au target was used to put two electrodes at 2 mm apart from each other following rf magnetron sputtering. The sputtering condition and optical image of as fabricated device has been shown in **Table 3.5** and **Fig. 3.8 (a, b)**.

**Table 3.5.** Au nanoparticle deposition conditions

<b>Target</b>	Au (99.99%)
<b>Target-substance distance</b>	8cm
<b>Base pressure</b>	10 mTorr
<b>RF power</b>	150 watt
<b>Deposition pressure</b>	8 mTorr
<b>Deposition temperature</b>	8 Kelvin
<b>Deposition rate</b>	1 nm /Sec

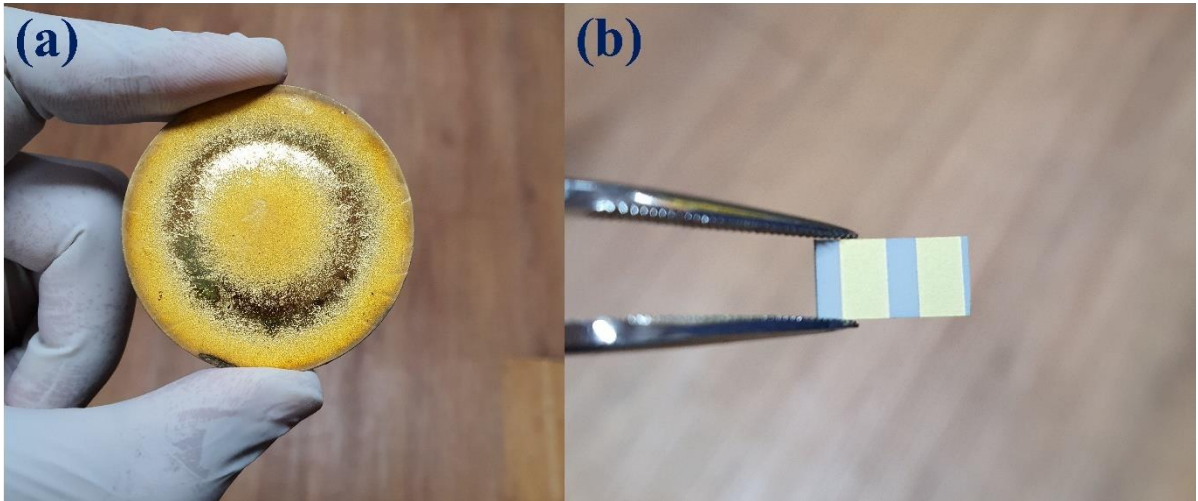


**Fig. 3.8.** (a) Au target (b) optical image of the as prepared device

### 3.6 The device fabrication process

An extremely rough alumina substrate ( $12 \times 6 \text{ mm}^2$ ) was washed for 5 minutes in ethanol, acetone, and isopropanol, then ultrasonicated for 15 minutes. ZnO (iTASCO, 99.99% purity) target was used in sputtering with an RF magnetron in an ultra-high vacuum chamber for depositing nanosized ZnO nanoparticles over alumina. A rapid thermal annealing process was used in a sequential manner to shape a permeation-supporting morphology and produce a stronger nanoparticles structure. Five different sensors were annealed at different temperatures (as-grown,  $800^\circ\text{C}$ ,  $900^\circ\text{C}$ ,  $1000^\circ\text{C}$ , and  $1100^\circ\text{C}$ ) for 5 minutes each using the rapid thermal annealing (RTA) method in an argon gas atmosphere (vacuum condition). The RF magnetron sputtering technique was then used to deposit a distinct thin film of optimized nanosized Pt metal with a high aspect ratio on the ZnO nanoparticles. And then again  $300^\circ\text{C}$  annealing temperature was also used for the same time which has been done after the ZnO annealing procedure time. The RF power and deposition time were used to monitor the metal deposition rate. For

clarification, each device was labelled as S0 = Pt@as grown ZnO NPs, S1= Pt@800°C annealed ZnO NPs, S2 = Pt@900°C annealed ZnO NPs, S3 = Pt@1000°C annealed ZnO NPs, and S4 = Pt@1100°C annealed ZnO NPs. The SCS 4200 probe station framework was used to investigate the rotating ohmic transmission of nanoparticles/alumina produced by gold (AU) electrodes opposite to one another at a gap of 2 mm. The entire schematic diagram is depicted in **Fig. 3.9**.

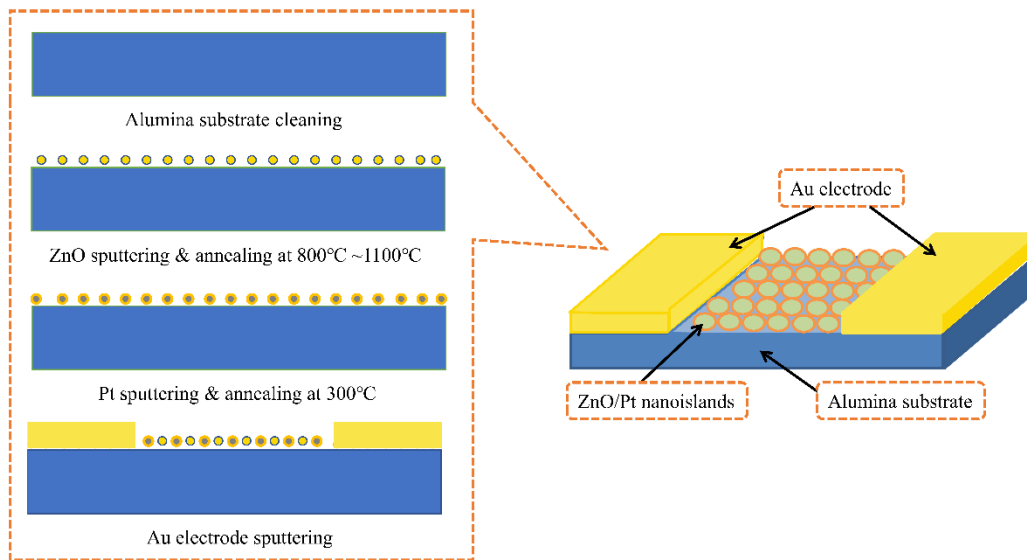


**Fig. 3.9.** Device fabrication process of ZnO-Pt hydrogen sensor.

### **3.7 Evaluation methods: Pt@ZnO nanoparticles decorated alumina substrate for stable gas sensor**

After confirming the optimum condition for stable hydrogen sensor, the device has been prepared for several evaluation methods including material characterization which is listed in the **Table 3.6**.

**Table 3.6.** Evaluation methods

SL No	Methods
1	Morphology evaluation
2	AFM
3	FESEM
4	XRD
5	Water contact angle
6	XPS
7	EDS elemental analysis
8	EDS mapping
9	For measuring electrical property check the dynamic response study
10	Measuring hydrogenation and dehydrogenation response magnitude
11	Transient response at different gas concentrations
12	Long term stability check at higher operating temperature
13	Selectivity check at different test gases

### 3.7.1 Atomic force microscopy

AFM is a high-resolution scanning probe microscopy that can photograph nanomaterials at fractions of a nanometer resolution, more than 1000 times greater than the optical diffraction limit. In this thesis, 3D atomic force microscopy (AFM, MultiMode V) was utilized to examine the roughness and RMS grain size of nanostructured ZnO nanoparticles.



### **3.7.2 FESEM (Field emission scanning electron microscopy)**

FESEM is a widely regarded microscopy instrument that can produce images with a resolution of less than 1 nm. A directed beam of electrons scans the sample's surface by communicating with its atoms, producing a variety of signals that can be observed, revealing details about the sample's topography and composition. In this thesis, Cold field emission scanning electron microscopy (Cold FE-SEM, SU8220) was utilized to study the surface morphology of ZnO/Pt nanoparticles on an alumina substrate under various annealing conditions.

### **3.7.3 X-ray diffraction analysis (XRD)**

The atomic and molecular composition of a crystal can be determined using x-ray diffraction techniques. Because of the crystalline atoms, electron beams diffract at various angles and intensities, resulting in a three-dimensional image of the atoms in the crystal. A high-resolution X-ray diffraction (XRD, D/MAX2500V/PC, Ulsan, Korea) with Cu K $\alpha$  ( $\lambda = 0.154$  nm) radiation over a two-dimensional screening spectrum of 10–90° was used to examine crystallite size and material composition of the nanoparticles.

### **3.7.4 Water contact angle system**

The hydrophobicity and surface energies of the nanomaterials were checked by Goniometry of contact angles (Kruss DSA 100 drop form analyzer, Ulsan, Korea) was used to calculate water droplet contact angles using the sessile drop technique at room temperature. A micro-syringe was used to drop deionized water droplets (approximately 5  $\mu$ L) on the thin film surfaces.

### **3.7.5 X-ray photoelectron spectroscopy (XPS)**

XPS is a highly surface sensitive measurement technique that evaluates the elemental composition, chemical state, electronic state, of the material at the parts per thousand range. It simultaneously measures the kinetic energy of a beam of x-rays and number of electrons that escape from the top 0 to 10 nm of the material. The electronic and chemical state of the metal interface with ZnO nanoparticles was analyzed by x-ray photoelectron spectroscopy (XPS, Thermo Fisher K-Alpha) with Al K $\alpha$  radiation as a medium of X-rays.

### **3.7.6 EDS elemental analysis and mapping**

Dispersive of energy X-ray spectroscopy offers chemical characterization as well as elemental and compositional knowledge about nanomaterials. All of the atomic and weight percent of the nanomaterials are given by the interaction of the excited x-ray source and the sample. It also includes a detailed x-ray emission spectrum for each element. In this thesis, energy dispersive X-ray spectroscopy (EDS, JEOL, JEM-2100 F) was used to examine the textural properties of the as-prepared samples.

### **3.7.7 Measuring gas sensing properties**

The hydrogenation and dehydrogenation properties were checked at a fixed temperature of 300°C against different H<sub>2</sub> concentrations to determine smooth response/recovery and stability properties. For all measurements and data processing, a Keithley probe station (SCS-4200) was used with a specified switching voltage of 1V, and a configurable heater installed with the device holder in the gas chamber. To control the concentration of hydrogen gas in synthetic atmosphere, an automated flow

rate monitoring system (GMC 1200, ATOVAC, Ulsan, Korea) was used. The gas mixture was maintained at a constant flow of 200 sccm on the fabricated device which was mounted on an integrated heater.

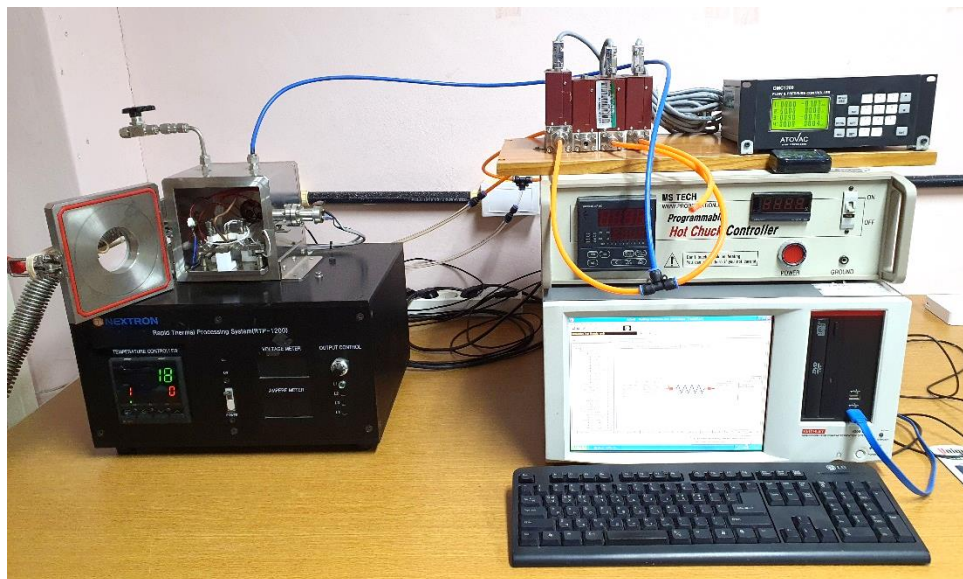


**Fig 3.10.** Hydrogenation and dehydrogenation measuring setup.

### 3.8 Summary

In this chapter, the experimental steps, and evaluations of ZnO nanoparticles based on Pt metal on alumina were described in this chapter. The structure of ZnO nanoparticles was demonstrated using detailed laboratory procedures. The decoration of Pt metal @ZnO nanoparticles was also described in detail. A system for hydrogenation and dehydrogenation, as well as a gas measuring system, was introduced. Characterization techniques for analyzing the morphology of nanomaterials, crystal consistency, metal oxide defects, and stable hydrogenation and dehydrogenation properties were described.

## Stable hydrogenation and dehydrogenation performance analysis of Pt@ZnO nanoislands decorated over alumina

## 4.1. Structural, morphological, and compositional characteristics

AFM images are used to examine the surface roughness of as-grown and annealed ZnO nanoparticles, as shown in **Fig. 4.1(a-e)** using  $300\text{ nm} \times 300\text{ nm}$  scan area.

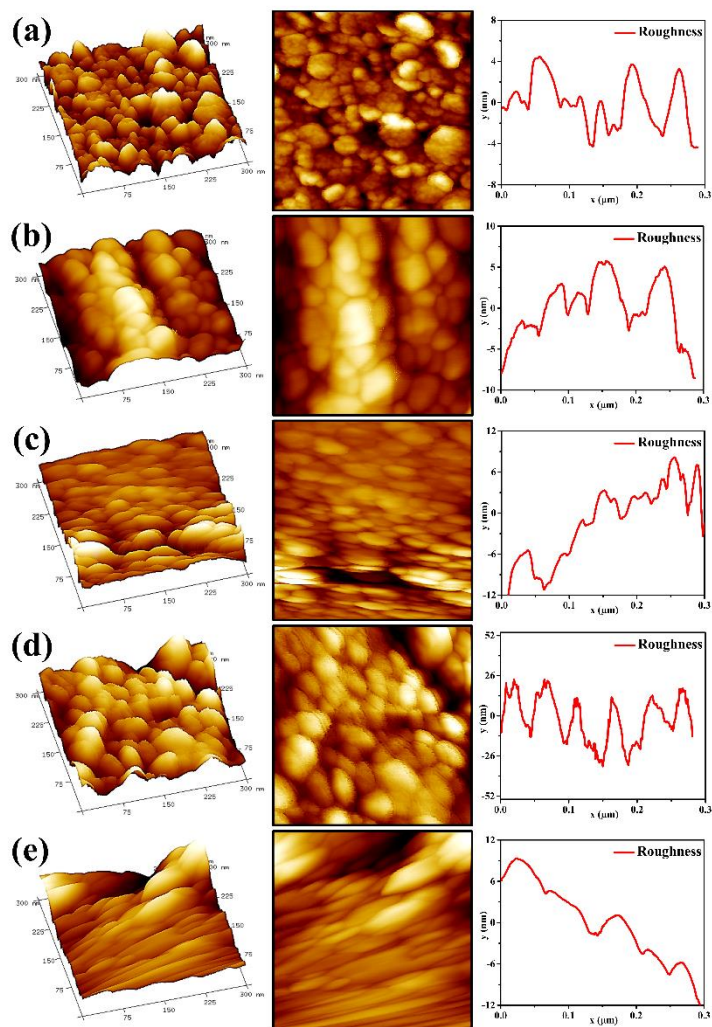


**Fig. 4.1.** AFM analysis of ZnO nanoparticles (a) as grown; (b)  $800^{\circ}\text{C}$ ; (c)  $900^{\circ}\text{C}$ ; (d)  $1000^{\circ}\text{C}$ ; and (e)  $1100^{\circ}\text{C}$ , respectively.

**Table. 4.1** summarizes the average grain size and roughness of the surface. All films have various nanostructures at different proportions, as seen in the AFM micrographs.

Every sample's surface roughness was calculated in five different locations. The roughness increases after raise the annealing temperature along with grain size increasing due to the more activation energy to atoms at higher temperature. Higher annealing conditions will energize grain size migration and allow more grains to coalesce during the annealing process. [31]. From AFM analysis (Fig. 4.1(d)) it was observed that ZnO deposited uniformly over the entire Al<sub>2</sub>O<sub>3</sub> surface.

**Table 4.1.** AFM Measurements for ZnO nanoparticles at different annealing conditions.

<b>Sample</b>	<b>Roughness (nm)</b>	<b>RMS Grain size (nm)</b>
<b>ZnO@alumina (non-annealed)</b>	5.83	4.70
<b>ZnO@alumina at 800°C</b>	8.15	6.67
<b>ZnO@alumina at 900°C</b>	11.61	9.38
<b>ZnO@alumina at 1000°C</b>	30.75	26.2
<b>ZnO@alumina at 1100°C</b>	10.53	9.43

The average grain size of these nanoisland was 30.75 nm with 26.2 RMS roughness. Fang et al. [32] also reported that at higher annealing conditions, sufficient energy should also be required for the molecules to gain in order for them to disperse and hold the proper site in the molecular structure, resulting in particles with lower surface energy, which also confirms in our contact angle analysis. However, as consistent, and compressed materials of nanostructure are formed during the nanoparticles prepared over the alumina substrate, as seen in Fig. 4.1(e), the roughness declines. Also, recrystallization happens as the calcinated temperature exceeds 1000°C, and the roughness of the ZnO surface decreases due to agglomeration. The surface roughness of the nanoparticles that were annealed up to 1000°C increased significantly. The gradual

increase in surface roughness could be the result of significant grain growth. The propagation loss is influenced by surface roughness, which is a significant factor. As a result, films that have been annealed at higher temperatures ( $>1000^{\circ}\text{C}$ ) are insufficient for ZnO@alumina devices.

**Fig. 4.2(1a-5a)** illustrates the representative morphological structure of the non-annealed sample (S0) and samples annealed at  $800^{\circ}\text{C}$ ,  $900^{\circ}\text{C}$ ,  $1000^{\circ}\text{C}$ ,  $1100^{\circ}\text{C}$  (S1-S4) revealed by the Cold FE-SEM images in an inert gas environment. A typical high resolution SEM image shown in the inset picture confirmed the formation of thin film layers consisting of several nanoparticles. It can be seen from the SEM images, that that a non-uniform nanoparticle appears on the film (Fig. 4.2(1a)). These non-uniform thin film distribution can produce unstable performance for any device [33]. Rota et al. [34] stated that, RTA simplifies the dispersion process of the metal surface, which ultimately increases the range of interface, alloy formation and nanoisland uniformity. Furthermore, these individual metal NPs clusters continue to diffuse with increasing annealing temperature (Fig. 4.2 (2a–5a)). From the SEM images, it was clear that the diffusion of metallic nano-islands begins at  $800^{\circ}\text{C}$  and continues to increase as the temperature increases, forming more uniform grain boundaries (Fig. 4.2 (2a-5a)). In Fig. 4.2 (4a), for the  $1000^{\circ}\text{C}$  annealed ZnO/Pt nanoparticles layers, thin layers of metal NPs were found to be uniformly distributed. Therefore, in Fig. 4.2 (4a) an improvement appears in the structural properties of the ZnO/Pt layers that is more homogeneous and simple than other samples, since at higher temperatures the molecules propagate and assume the right position in the crystal lattice and increase the grain size [35], which also confirms in the AFM images of Fig. 4.1(d). The radius distributions reported in Fig.

4.2(1b–5b) for the ZnO nanoparticles before annealing and ZnO annealed at 800°C, 900°C, 1000°C and 1100°C respectively, indicate a Gaussian distribution around a radius mean value. It could be seen that the nanoisland aligned in random orientations and the average diameters of the nanoparticles were about 46.23 nm, 47.29 nm, 53.39 nm, and 53.74 nm for sample S0, S1, S2 and S4, respectively. However, after the contacting with more energy at higher temperatures the nanoparticles are placed in a modified homogeneous nanoparticle, of which the average diameter changed to approximate 55.03 nm for sample S3 as shown in Fig. 4.2(4b).

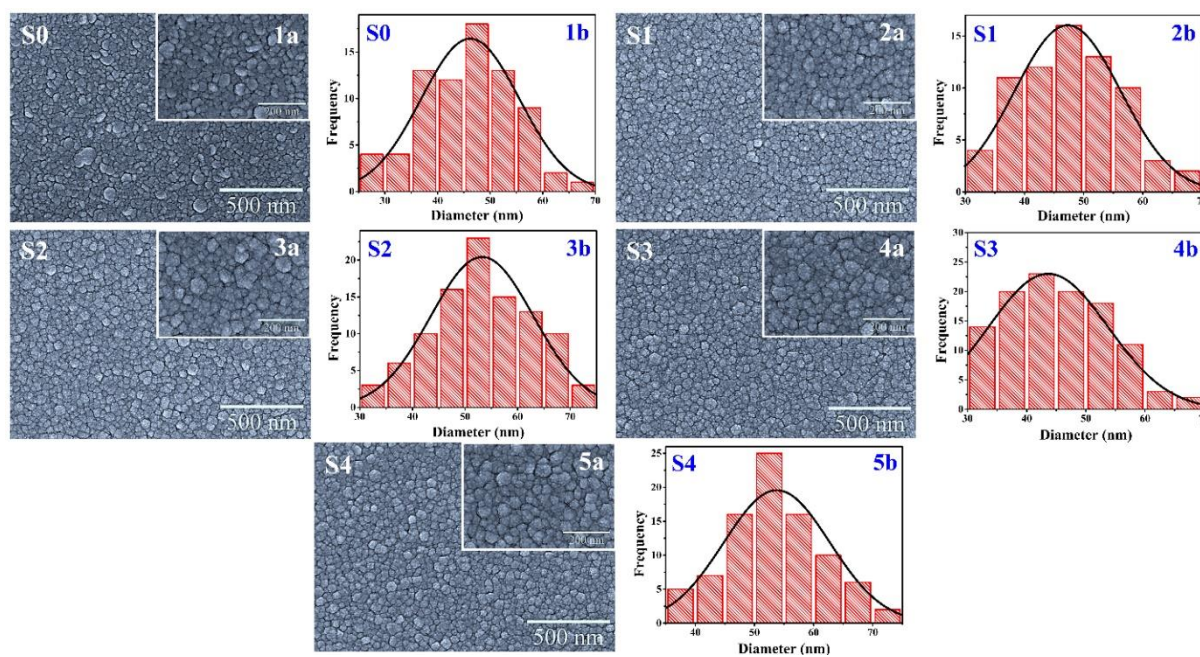


**Figure 4.2.** FE-SEM surface analysis for sample (S0-S4); (1a-5a) Surface morphologies of ZnO-Pt (inset higher magnification images) and (1b-5b) radius distribution for each sample.



At a temperature of 1100°C, ZnO nanoisland becomes unstable from the substrate and this phenomenon will become more apparent with increasing temperature. It is also conceivable that at high temperatures, the rough alumina substrate becomes incredibly soft, making it impossible to have a robust interface for ZnO molecule diffusion, as seen in Fig. 4.2 (5a). Thus, we conclude that the molecules of our ZnO nanoisland are higher than 1100°C enough to destabilize the rough alumina from the substrate, resulting in the aggregation of nanostructures on the substrate.

A typical high resolution XRD spectrum technique scanned from 20° to 90° (2θ) continuously for the as grown and annealed ZnO thin films for 800°C, 900°C, 1000°C and 1100°C respectively as shown in **Fig. 4.3(a)** and Pt@1000°C annealed ZnO nanoisland over alumina substrate is depicted in **Fig. 4.3(b)** for the pre- and post-annealing cases. It can be seen from the Fig. 4.3(a) that, the most intense peak located at  $2\theta = 57.51^\circ$  due to ZnO (110) diffraction planes of cubic phase which is in pm-3m space group (JCPDS: # 01-080-4983). Diffraction peaks at  $2\theta = 34.29^\circ$  (JCPDS: # 01-075-1533) are for ZnO (002) hexagonal wurtzite phase (Fig. 4.3(a); as-grown) which was discovered to be intensified for further annealed sample (Fig. 4.3(a); 800°C, 900°C, 1000°C and 1100°C respectively) and  $2\theta = 66.53^\circ$  is also for ZnO (112) phase are in the space group of P63mc. An increase in kinetic energy occurred due to annealing at 800°C to 1000°C which enhances the intensity of (002) peak.

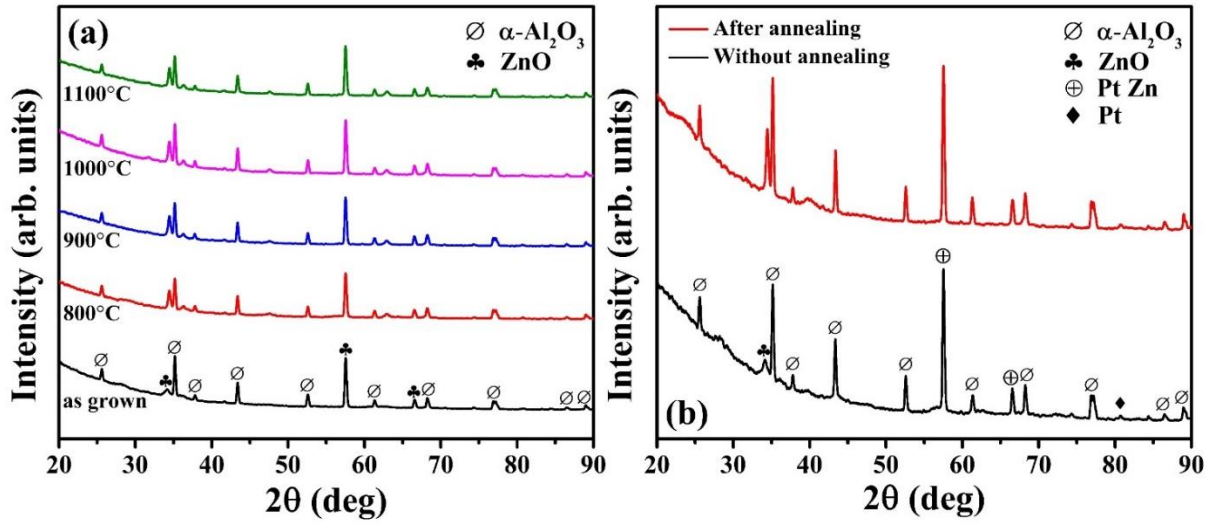


**Fig. 4.3.** XRD analysis of (a) as-grown and annealed at 800°C; 900°C; 1000°C; 1100°C; ZnO NPs respectively (b) ZnO-Pt nanoparticles before and after annealing.

At higher annealing temperature atoms mobility enhances which gives the better structure improvement by gaining additional kinetic energy for reducing the defects and achieving improve internal order [35]. However, the (002) peak intensity decreases after annealing at higher temperature (1100°C). In comparison to film grown before annealing, the full width half maximum of the (002) peak reduces after annealing, as seen in **Table. 4.2**. It confirms that annealing improves crystalline order by eliminating defects including vacancies and lattice disorders. The Scherrer formula can be used to measure the crystalline grain size from the FWHM of the (002) diffraction peak [36] :

$$D = \frac{0.9\lambda}{\beta \cos\theta} \quad (4.1)$$

Where  $\lambda = 1.540 \text{ \AA}$  is the wavelength of the X-rays,  $\beta$  is the full width half maximum intensity of the distinctive peak, and  $\theta$  is the Bragg's angle. Diffraction peak at  $2\theta = 25.61^\circ, 35.15^\circ, 37.76^\circ, 43.38^\circ, 52.55^\circ, 61.32^\circ, 68.23^\circ, 77.24^\circ, 86.5^\circ$  and  $88.99^\circ$  are

from  $\alpha$ -Al<sub>2</sub>O<sub>3</sub> (012), (104), (110), (113), (024), (122), (300), (119) and (312) respectively (JCPDS: # 00-046-1212). There was no other diffraction peak is found from as grown to annealed sample which indicates that the ZnO has high purity and good crystallinity. Furthermore, after the deposition of sensing layer, it can be seen from Fig. 4.3(b) that there was a small peak at  $2\theta = 80.73^\circ$  correspond to the Pt (114) planes of the tetragonal crystal structure which indicates the Pt coating over ZnO nanoisland has been successfully carried out. Peaks at  $2\theta = 57.51^\circ$ ,  $66.53^\circ$  are related to the (112) and (220) of platinum zinc for tetragonal crystal lattice of P4/mmm space group which maybe originated from the metal alloy and formation of Pt nanoparticles with Zn. The transformation of ZnO-Pt into PtZn alloy is done through the formation of Zn by hydrogen reduction, chemisorption on the surface of Pt nanoparticles and diffusion of Zn to the bulk Pt nanoparticles to produce larger PtZn nanoparticles [37].

**Table. 4.2.** XRD analysis of 002 peak of ZnO NPs prepared at different annealing conditions.

Phase	Sample	Peak Position ( $2\theta$ )	FWHM	Crystallite Size (nm)	d-spacing ( $\text{\AA}$ )
ZnO (002)	as grown	34.29	0.65	12.78	2.62
	800°C	34.46	0.34	24.46	2.60
	900°C	34.46	0.33	25.20	2.60
	1000°C	34.46	0.32	25.99	2.60
	1100°C	34.47	0.31	26.83	2.59

To investigate the surface energy and solubility of various ZnO nanoparticle morphologies, contact angle were measured by diiodomethane (**Fig. 4.4 (a, c, e, g, i, k)**) and DI water (**Fig. 4.4 (b, d, f, h, j, l)**) droplets as per Young's theory who suggested a normalization equation of three intermolecular surface energies.

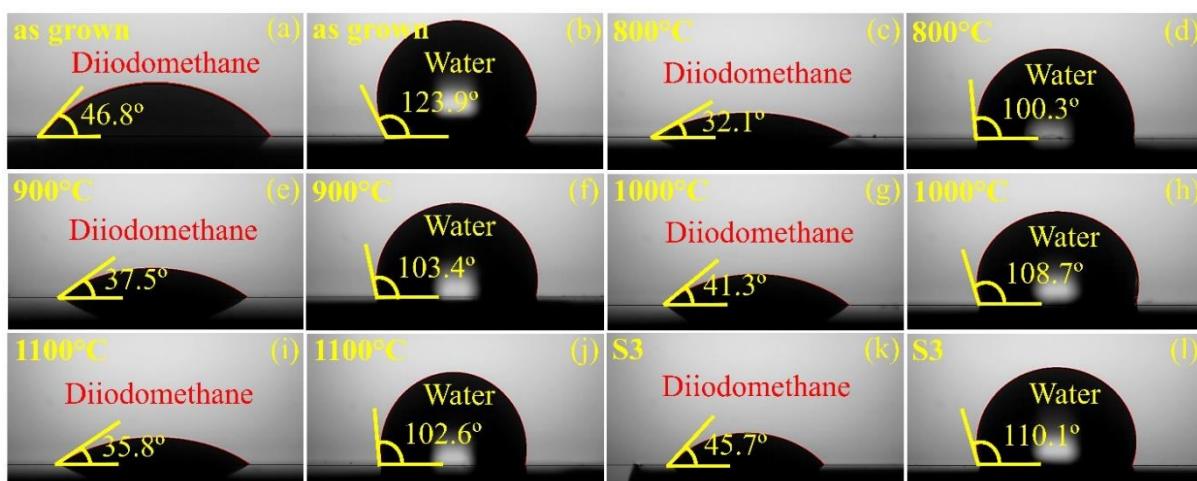


**Fig 4.4.** Contact angle analysis of ZnO nanoparticles; (a, b) as grown; (c, d) 800°C; (e, f) 900°C; (g, h) 1000°C; (i, j) 1100°C and (k, l) sample S3; for diiodomethane and water, respectively.

It is widely known that a surface is hydrophobic if the contact angle is greater than 90 degrees, and hydrophilic if the contact angle is less than 90 degrees. As a result, all the samples are hydrophobic. Therefore, the molecules of water do not stick to the surface and the reaction size can be slowed down, so stable performance can be provided with H<sub>2</sub> gas [38]. It is interesting to note that the contact angle is proportionate to the roughness of the surface but inversely proportionate to the strength of the surface. From AFM measurements it is observed that during annealing, the root mean square grain size is found to increase, which also includes a gradual increase in RMS roughness (Table 1), which can also be used to determine the samples hydrophobicity. Contact angle measurements show a gradual increase in hydrophobicity with increasing annealing temperature. Furthermore, hydrophobicity is inversely proportionate to the film surface energy [39]. The following equation (Fowkes theory) [40] was used to calculate surface energy, which is outlined in **Table. 4.3.**

$$\gamma_l(\text{Cos}\theta+1)/2 = \sqrt{(\gamma_l^d)(\gamma_s^d)} + \sqrt{(\gamma_l^p)(\gamma_s^p)} \quad (4.2)$$

Initially diiodomethane is used, with a total interfacial tension of 50.8 mN/m and no polarization part, this material has a comparatively high total surface tension. The contact angle and dispersion element obtained by the diiodomethane liquid can thus be used to calculate,  $\gamma_s^d$ .

$$\gamma_s^d = (\gamma_l/4) (\text{Cos}\theta+1)/2 \quad (4.3)$$

Later, water with a non-scattered (polar part) such as  $\gamma_l^p = 46.4$  mN/m, and  $\gamma_l^d = 26.4$  mN/m can be used in conjunction with the contact angle on the solid sensor's surface to find the  $\gamma_s^p$ . Finally, Eq 6 can be used to quantify total surface energy.

$$\gamma_s = \gamma_s^d + \gamma_s^p \quad (4.4)$$

Where  $\gamma_l, \gamma_s, \gamma_l^d, \gamma_l^p, \gamma_s^d, \gamma_s^p$  represents the energies at the surface of liquid, solid, dispersive, polar components of liquid and solid, respectively.

**Table 4.3.** Calculation of contact angle and surface energy for various annealing surfaces of ZnO nanoparticles.

Sample	Contact angle (Diiodomethane)	Contact angle (Water)	$\gamma_s$ (mN/m)	$\gamma_s^d$ (mN/m)	$\gamma_s^p$ (mN/m)
ZnO@alumina (non-annealed)	46.8°	123.9°	40.73	36.04	4.69
ZnO@alumina at 800°C	32.1°	100.3°	43.66	43.33	0.33
ZnO@alumina at 900°C	37.5°	103.4°	41.36	40.85	0.51
ZnO@alumina at 1000°C	41.3°	108.7°	40.11	38.95	1.16
ZnO@alumina at 1100°C	35.8°	102.6°	42.14	41.66	0.48
Pt@1000°C annealed ZnO nanoparticles on alumina	45.7°	110.1°	37.75	36.63	1.11

**Table 4.3** shows that the minimal quantity of surface energy (37.75 mN/m) was observed for Pt@1000°C annealed ZnO nanoparticles at a maximum contact angle of 110.1°. This is consistent with the ratio of hydrophobicity to contact angle. The energies of the sample surface gradually decrease as the annealing temperature increases as the contact angle gradually increases. The improved rough surface of the ZnO NPs thin layer may result in reduced surface energy. The size of the RMS grain size illustrates the increasing trend of higher annealing temperatures, which also confirms in AFM and SEM measurements.

XPS calculations were used to validate the existence of Pt and the direction of electron transfer through the ZnO-Pt interface on samples after synthesis (S0-S4). In **Fig. 4.5** shows the corresponding doublets of the nuclear core levels Pt 4f, O 1s, Zn 2p, which are deconvoluted into Pt 4f<sub>5/2</sub>, Pt 4f<sub>7/2</sub>, O 1s, Zn 2p<sub>3/2</sub>, Zn 2p<sub>1/2</sub> by the

adjustment method Gauss-Lorentz after linear subtraction from the background. For sample S0 (Fig. 4.5, (1a-1c)) XPS spectra of the central level of Pt 4f<sub>5/2</sub>; 69.05, Pt 4f<sub>7/2</sub>; 72.41, O 1s; 529.04, Zn 2p<sub>3/2</sub>; 1019.19, Zn 2p<sub>1/2</sub>; 1042.30 eV is observed [41,42]. It was discovered that the center scales binding energy of Pt, O, Zn in samples S1-S3 (Fig. 4.5) is shifted from a lower binding energy to a higher binding energy (Table. 4.4).

**Table. 4.4.** Study of XPS measurements for sample S0~S4.

<b>Sample</b>	<b>Pt 4f<sub>5/2</sub> (ev)</b>	<b>Pt 4f<sub>7/2</sub> (ev)</b>	<b>O 1s (ev)</b>	<b>Zn 2p<sub>3/2</sub> (ev)</b>	<b>Zn 2p<sub>1/2</sub> (ev)</b>
<b>S0</b>	69.05	72.41	529.04	1019.19	1042.30
<b>S1</b>	69.28	72.67	529.06	1019.30	1042.38
<b>S2</b>	69.61	72.97	529.28	1019.45	1042.52
<b>S3</b>	70.62	73.98	530.73	1020.93	1044.04
<b>S4</b>	69.21	72.60	528.98	1019.23	1042.30

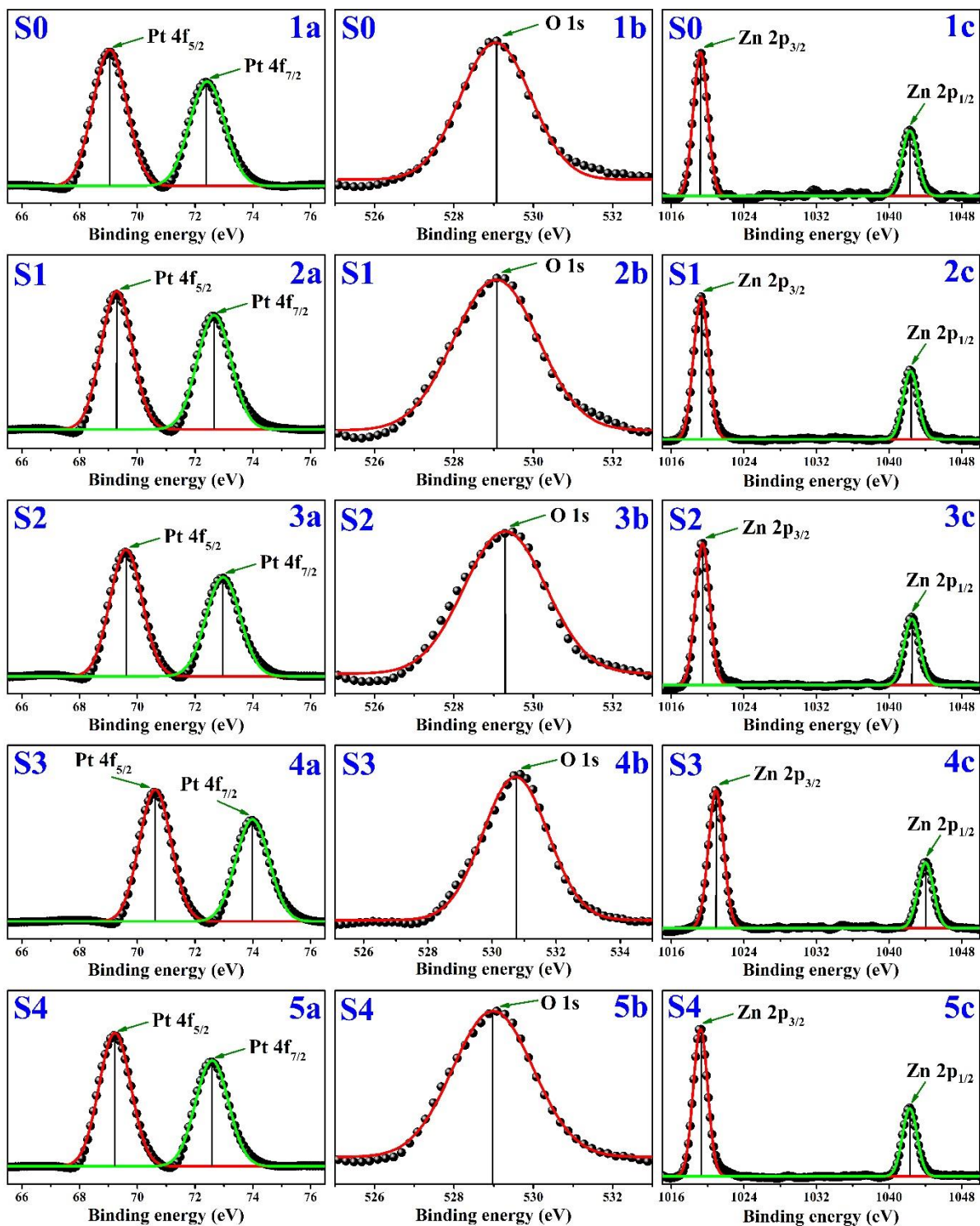


**Fig. 4.5** XPS analysis for the sample S0 (1a, 1b, 1c); S1 (2a, 2b, 2c); S2 (3a, 3b, 3c); S3 (4a, 4b, 4c); S4 (5a, 5b, 5c), respectively.



Maximum displacement at higher binding energies for Pt 4f<sub>5/2</sub>; 70.62, Pt 4f<sub>7/2</sub>; 73.98, O 1s; 530.73, Zn 2p<sub>3/2</sub>; 1020.93, Zn 2p<sub>1/2</sub>; 1044.04 eV was observed for sample S3 annealed at 1000°C (Fig. 4.5, (4a-4c)). Therefore, the BE in terms of positive displacement changes, We assume that as electrons come into contact with each other, they pass from ZnO to Pt [43]. However, at a higher annealing temperature (1100°C) for sample S4, the binding energies decrease for the Pt, O and Zn spectra (Fig. 4.5, (5a-5c)), which may be due to weak coupling of ZnO nano-islands with Pt nanoparticles, since the separation caused by temperature diffusion is greater [44]. Overall, XPS measurements confirm that nanoparticles are tightly bound to each other at 1000°C, increasing the permeation pathway [39].

An analysis of the elemental composition of EDS **Fig. 4.6(a)** was performed for samples S3, which confirms the mass and atomic percentages of metallic nanoparticles (Al, O, Zn, Pt). The presence of aluminum oxide (Al), oxygen (O), zinc (Zn), platinum (Pt) and the lack of contamination-related peaks indicates the development of a surface structure of high purity to stabilize the detection properties of hydrogen gas. The EDS mapping for sample S3 is seen in **Fig. 4.6(b)**, indicating high purity of a properly prepared sample with uniform ZnO-Pt distribution across the substrate.

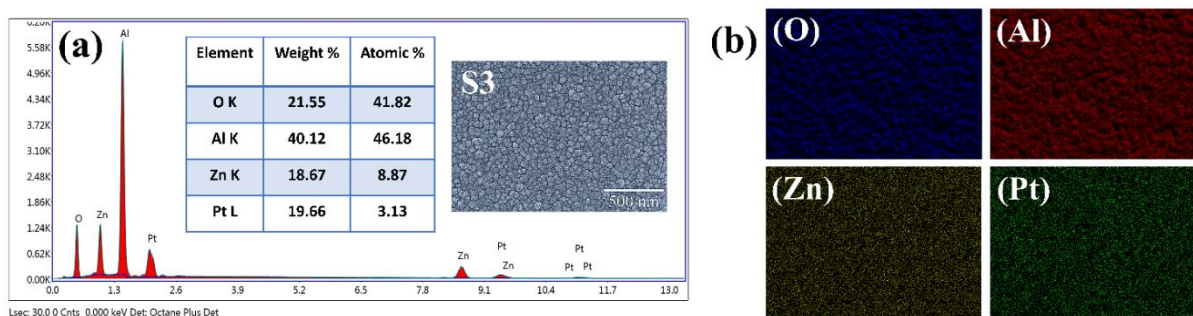
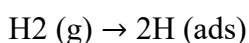


**Fig. 4.6.** EDS (a) elemental (b) mapping analysis for S3 sample

## 4.2. Gas sensing properties of ZnO/Pt NPs:

The sensing measurement setup for highly stable high temperature (300°C) hydrogen gas properties is shown in **Fig. 4.7**. The sensing properties of ZnO-Pt NPs layers on an alumina substrate have been observed because of resistance shift when exposed to various concentrations of hydrogen (H<sub>2</sub>) gas. Previous studies have reported that gas detection characteristics can be affected by operating temperature and catalytic load [45]. For example, the interaction at the surface of hydrogen and chemisorbed oxygen on ZnO-Pt NPs sensors can be influenced by working temperatures. Furthermore, a small volume of catalyst is insufficient for effective catalytic correction. However, due to the saturation of the catalyst sensor and the accumulation of the catalyst, an excess of the catalyst may cause a deterioration in the gas measurement activity [46]. Hydrogen molecules are physisorbed on the surface of Pt in synthetic air and eventually dissociate into hydrogen atoms, which are chemisorbed in Pt's lattice structure to form Pt hydride (PtH<sub>x</sub>) as follows:



The introduction of hydrogen atoms into the Pt lattice induces a lattice expansion in PtH<sub>x</sub>, and the H atoms serve as electron-scattering sources, disrupting the free electron movement in Pt atoms and altering the resistance, enhance the stability and reliability of a hydrogen sensor. Platinum has been described as a good catalyst for the formation of hydrides, a reaction that limits the rate of reaction of hydrogen under maximum thermal conditions ( $\geq 100^\circ\text{C}$ ) [47]. Selecting the most appropriate hydrogen sensor and determining its stability at a constant operating temperature (300°C), the

responses of non-annealing and varying the annealing parameters Pt loaded ZnO@alumina was measured. **Fig. 4.8** shows the representative dynamic response (conductivity vs. time) of five different sensors S0-S4 (a-e) to 1000 ppm H<sub>2</sub> at an operating temperature of 300°C. The S3 device provide repeatable and responses that are consistent throughout the transformation between H<sub>2</sub> exposure and air, as seen in Fig. 4.8(e). As the S3 sensor is subjected to various concentrations of H<sub>2</sub>, the resistance scale drops dramatically, which is congruence with the n-type semiconductor gas sensor characteristic. While removing the H<sub>2</sub> flow from the gas chamber and replacing it with just air, the resistance factor returns to its original value after a significant period, which then continues for repeated gas exposure cycles.

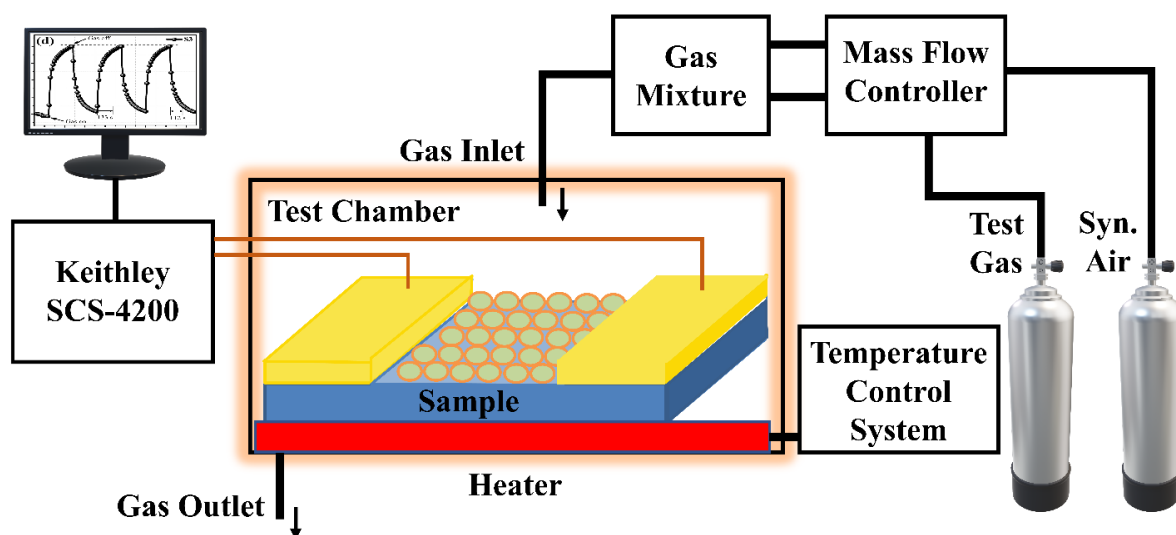


**Fig. 4.7.** Schematic setup of high temperature (300°C) hydrogen sensor testing.

In addition, the ZnO/Pt (S3) stabilized nanoisland sensor has a lower initial resistance (~132.5  $\Omega$ ) and faster response (133 s)/recovery (112 s) than other sensors, that is to say the distribution of the nanoparticles influenced by deposition layer, plays a key role in

the sensory efficiency. On the nano-porous sensing surface (S3), the hydrogen-induced lattice expansion (HILE) mechanism allows for a rapid charge transfer between absorbing H<sub>2</sub> gas and metal atoms. When performing charge exchange, because of synergistic effects and the large active surface, a strong coulomb scattering mechanism will build up charges inside the metal ZnO/Pt lattices. These observations are consistent with surface analysis by AFM and SEM (Figs. 4.1 and 4.2). We believe that a small number of ZnO/Pt nanoislands, located at closer distance from each other, with a good interispiatic catalytic structure enhance the synergistic effect regarding the absorption and desorption of hydrogen gas. Due to percolating channels with a good interface morphology, high degree of optimization is formed that can eventually enhance the Coulomb diffusion process (Figure 4.8(d)). Therefore, a faster absorption and desorption of hydrogen occurs, and this phenomenon concludes that the connectivity between the ZnO nanoparticles and the metal particle is decreased because of the annealing temperature-induced diffusion mechanism. In addition, the highly stable ZnO/Pt NPs layers facilitate to separate H<sub>2</sub> atoms very quickly and broaden the diffusion of scattered electrons within the metal lattice. This charge dispersion process is carried out continuously by H<sub>2</sub> residues within the metal lattice, while the metal is replaced by an insulating phase change [39,48].

Nanoparticle facilitated polymers or responsive thin films are well known for having low reaction diffusion coefficient. As a result, it aids in the improvement of H<sub>2</sub> gas adsorption and raises the reaction strength on the sensor surface. As a result, it is advantageous for rising H<sub>2</sub> adsorption process and the amount of the response on the sensor surface. However, in this case non-annealed ZnO/Pt membranes such as S0 may

reduce the gas response and transient base impedance, since the main conduction path through the Pt membrane is much higher than that of the diverse ZnO nanoislands [49]. On agglomerated sensing surfaces (S1, S2), (at 800°C and 900°C annealed), the hydride-induced expansion of the volumetric network might not be designed enough to bind the percolation paths and adjust the surface resistance quickly. Therefore, the opaque and weak catalytic interaction on bulk permeated surfaces can reduce the speed of overall detection process. In the sensor (S1, S2), a limited catalysts reaction was performed because the aggregation between Pt, ZnO NPs, which cannot provide higher hydrogen detachment.

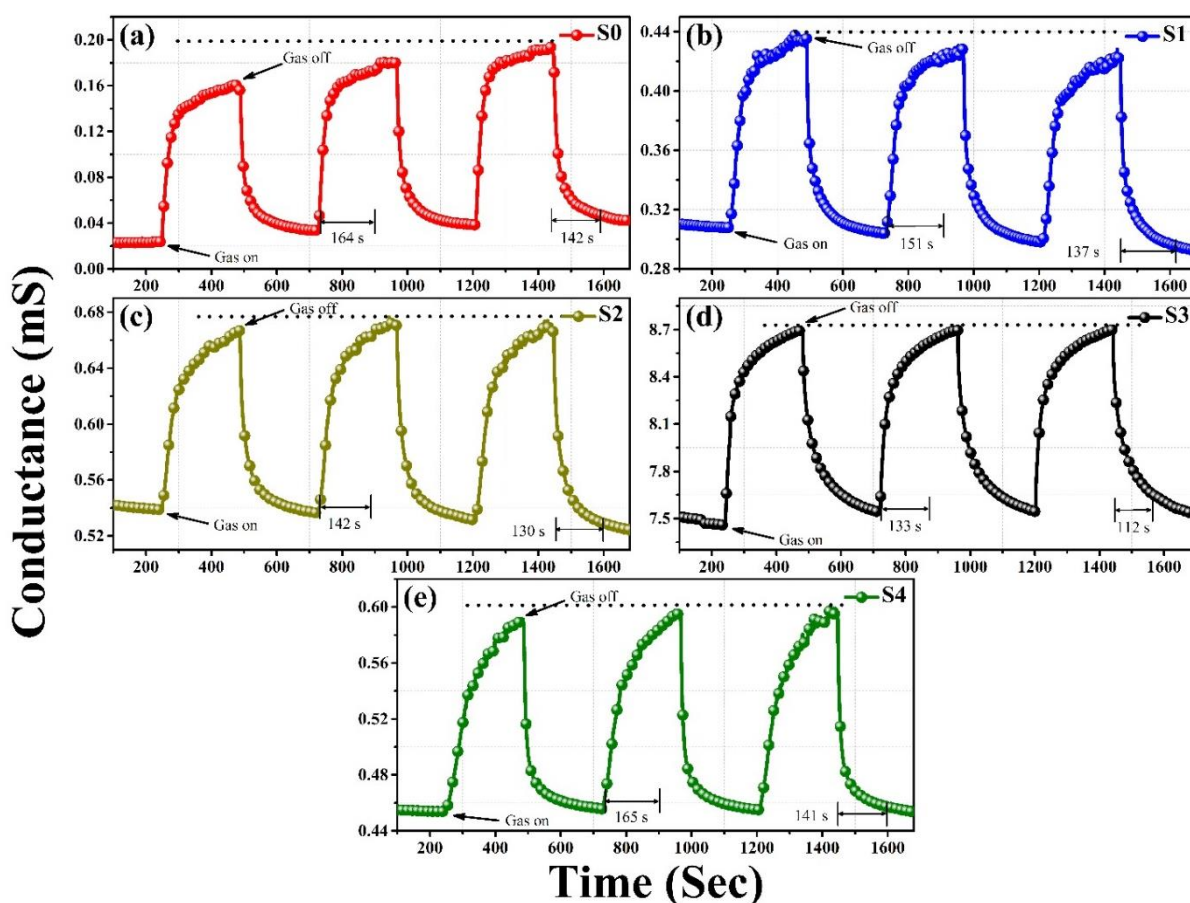


**Fig. 4.8.** Response-recovery time and stabilize sensor performance analysis of the samples S0-S4 (a-e) at 1000 ppm at high temperature (300°C) hydrogen gas.

The device did not show a fast catalytic reaction at high annealing temperature (S4), which can be explained using the structural analysis. The thin film morphology of incompatible ZnO-Pt metal NPs was verified by FE-SEM and XPS using higher annealed devices (S4), which decreased the number of total gas absorption areas, also lowering detection ability. This was verified by measuring the water contact angle and surface energy, and the sample had a lower surface roughness. It should also be remembered that the ZnO interface has the least surface roughness (Fig. 4.2(e)) increases the initial surface resistance and reduces the scattering of physically and chemisorbed H atoms. The result was the slowest and most unstable sensory behavior on the S4 device (Figure 4.8(e)). The smooth texture dynamic response and the hydrogenation/dehydrogenation process are worth mentioning here. As a result, at 300°C, high-frequency magnetron sputtering deposited ZnO-Pt nanoparticles on aluminum oxide demonstrate reaction and recovery times of 165/141 seconds (1% H<sub>2</sub>), with an average surface resistance of 2.19 kΩ (Fig. 4.8(e)). The increased resistance may be due to weak ZnO nanoparticle connections on the coarse alumina substrate. Therefore, weaker response and recovery time were observed due to the non-penetrated nanoparticles which cannot contribute significantly to hydrogen-induced lattice expansion. [42,44,46].

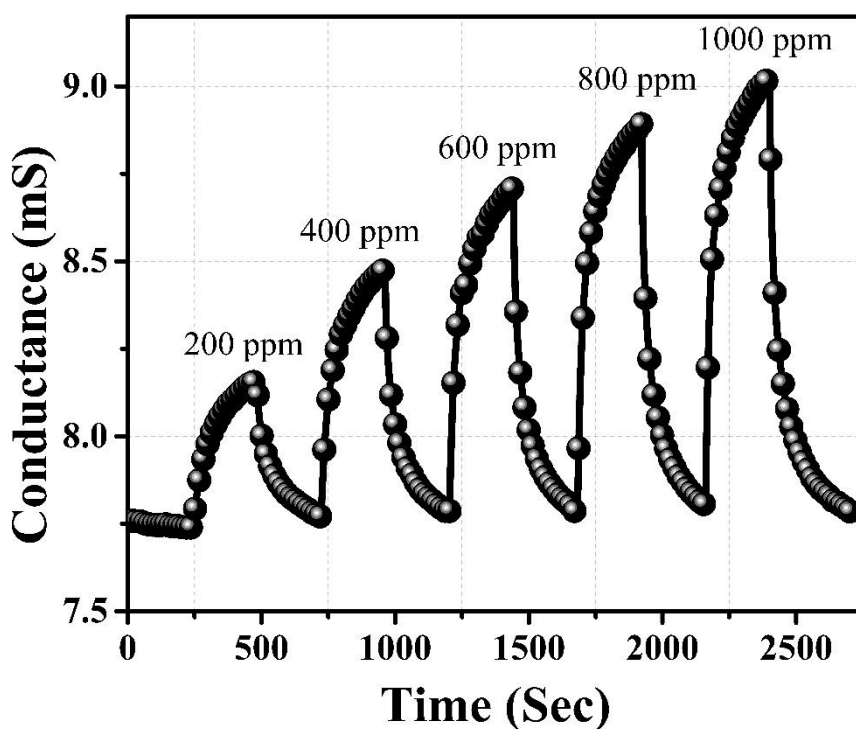


**Fig. 4.9.** Transient response characteristics of S3 (200-400-600-800-1000 ppm) at 300°C working temperature.

**Fig. 4.9** shows the transient response operation for sample S3 at different H<sub>2</sub> concentrations (200~400~600~800~1000 ppm) at high temperature (300°C). From this figure, we can see that there is a smooth response and recovery characteristics without any noise at high temperature H<sub>2</sub> concentrations, and the sensor response increases with increasing concentration. Repeatability is a crucial factor in assessing the reliability of a sensor device. In Fig. 4.8(d), the repetition of the S3 sensor was tested in the 1000 ppm H<sub>2</sub> concentrations at 300°C for three reaction/recovery cycles, which were also recorded without any hysteresis effect.

Long-term stability of sensor devices is very important for nearly all realistic technology. Gas response and base resistance were registered at 1000 ppm H<sub>2</sub> to measure the sensor's long-term stability for at least 30 days at optimum temperature (300°C) and the results obtained are shown in **Fig. 4.10 (a, b)**. The base resistance and reaction of the S3 sensor toward 1000 ppm H<sub>2</sub> diminished by almost less than 1% and 5%, respectively, after 30 days in comparison to its unique execution, which affirming its great steadiness. Within the light of such fabulous detecting properties, it has been concluded that the current device will show promise as an H<sub>2</sub> sensor that operates at a temperature.

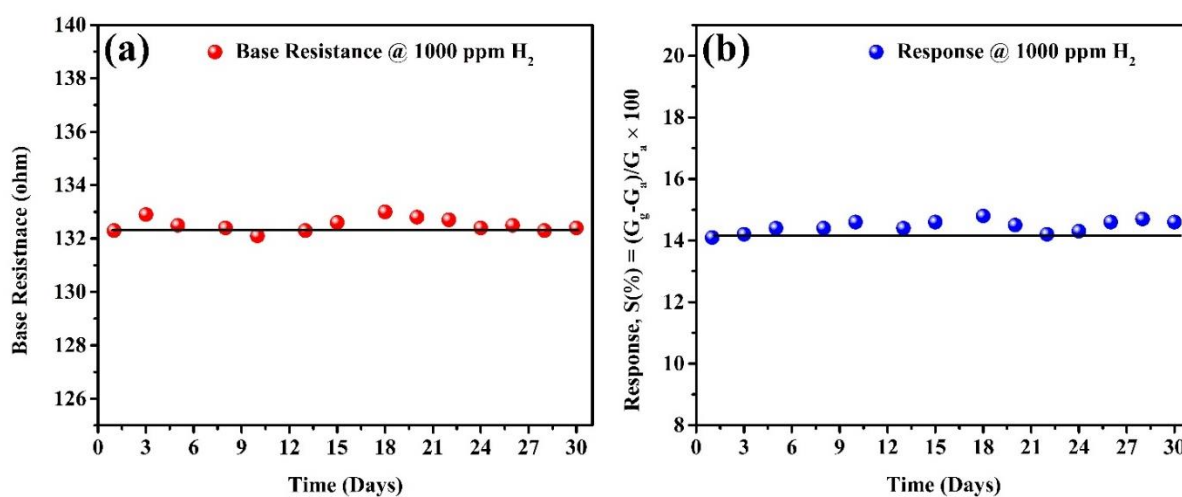


**Fig. 4.10.** Long term stability of the S3 sensor in case of (a) base resistance and (b) response, exposed to 1000 ppm H<sub>2</sub> gas at 300°C working temperature.

The linear relationship between the sensory reaction and the square root of hydrogen was investigated using the Langmuir isotherm principle of dissociative gas adsorption (**Fig. 4.11**). Through integration, H<sub>2</sub> ions chemically shift the charge on the surface (S<sub>M</sub>) to the concentration of the sensing material (ZnO/Pt) in a proportional



manner to the partial penetration of hydrogen ( $\theta$ ) [50]. Therefore, the change in resistance  $R_g/R_a$  is proportional to  $\theta$ . The dissociation reaction of  $H_2$  molecules on the surface of the sensor material can be expressed as follows.



Here,  $S_M$  represents the accessible area of the sensitive surface and is assumed to be proportionate to  $(1 - \theta)$ . According to isotherm hypothesis of Langmuir, in the state of equilibrium,

$$\frac{\theta}{(1 - \theta)} = \sqrt{\left(\frac{K_a}{K_d}\right)} \times \sqrt{P} = \sqrt{K} \times \sqrt{P} \quad (4.6)$$

Where the absorption and desorption considerations are  $K_a$  and  $K_d$ , respectively, and the fractional weight of hydrogen is  $P$ . The change in resistance is determined by the expression of low hydrogen ranges ( $\theta \ll 1$ ),

$$\frac{R_a}{R_g} \approx \theta \approx \frac{\theta}{(1 - \theta)} = \sqrt{K} \times \sqrt{P} \quad (4.7)$$

Where,  $R_g$ ,  $R_a$  represents the resistance to hydrogen absorption, the resistance in air (base resistance) and the equilibrium balance of  $K$  is constant and is equal to the hydrogen concentration at high pressure with hydrogen gas. Between the square root of the sensory response ( $S\%$ ) and the concentration of hydrogen, Fig. 4.11 is for fabricated sensors S3.

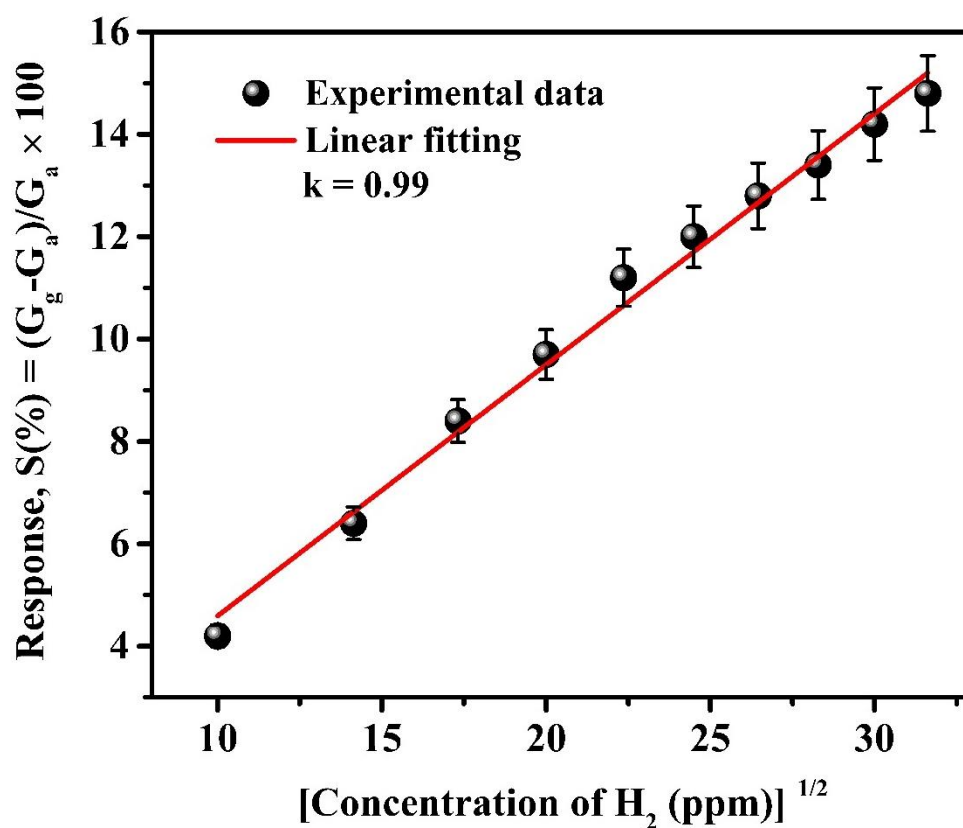


Fig. 4.11. Sensor linear correlation according to the Langmuir model.

The selectivity property of the S3 sensor could be seen in **Fig. 4.12** when it is exposed to 1000 ppm test gases at 300°C, which include H<sub>2</sub>, O<sub>2</sub>, CO, NO, CH<sub>4</sub>, and C<sub>3</sub>H<sub>8</sub>. With exception of H<sub>2</sub>, none of the gases elicited responses  $\geq 0.5$  percent (maximum 14.9% at 1000 ppm). Due to the high selectivity of ZnO-Pt catalysts with H<sub>2</sub> molecules, the as-fabricated sensor displayed excellent selectivity against H<sub>2</sub>. Catalytic behavior of the S3 sensor against H<sub>2</sub> deterioration can be highly alleviate and may be a surface phenomenon at a foremost temperature of 300°C, in which comparison to other test gases, adequate surface energy of the sensor surface aided properly in being reacts even with electron density of H<sub>2</sub>.

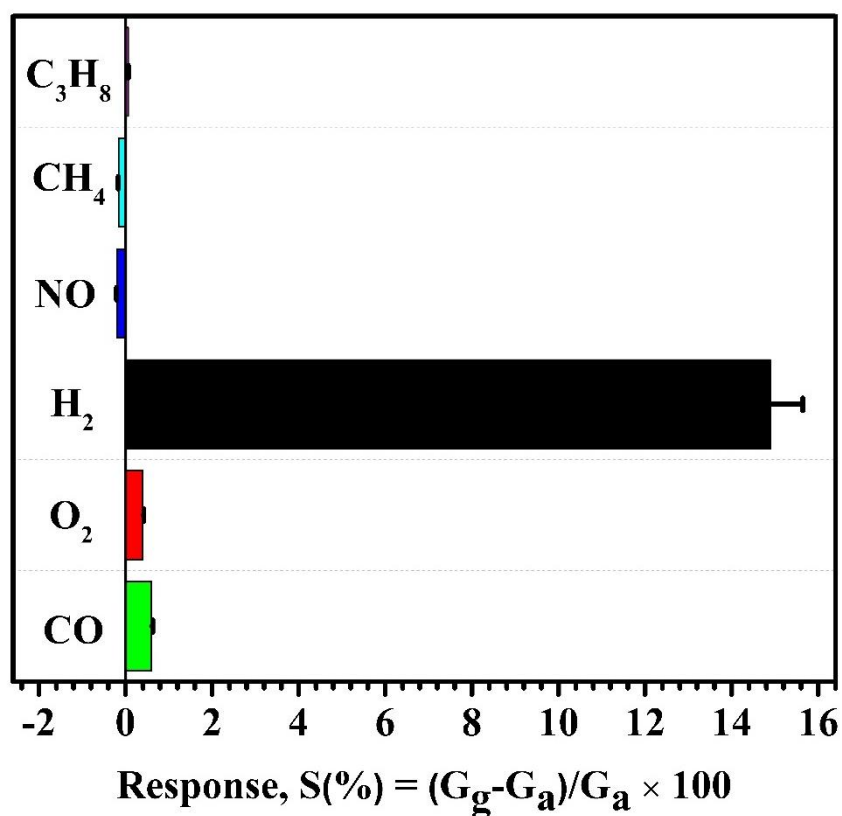


Fig. 4.12. Sample S3 selectivity histogram for different test gases.

### 4.3. Summary

In this chapter, the effects of surface diffusion during thermal annealing on ZnO morphology, as well as the loading of Pt metal@ZnO NPs and their catalytic properties at higher working temperatures for stable hydrogenation and dehydrogenation, were thoroughly investigated.

The results show that thermally annealed ZnO nanoislands with a Pt metal structure have improved catalytic morphology and stable hydrogenation and dehydrogenation efficiency when annealed to 1000°C.

The main points of this chapter are summarized below:

- The properties of a resistivity type stable high temperature hydrogen sensor based on Pt@ZnO nanoislands decorated over an alumina substrate have been developed.
- The intermetallic catalytic alloy forming with Pt metal is improved by improving the morphology of ZnO nanoislands.
- An improved Pt catalyst increases the surface charge density, which increases the gas absorption surface's hydrophobicity.
- A smooth response/recovery time of 133/112 sec at a concentration of 1000 ppm H<sub>2</sub> with a response magnitude of 14.9% (300°C) was achieved.
- Good repeatability and good range of detection (100-1000 ppm H<sub>2</sub>) are achieved.

# CHAPTER 5

---

## Conclusions and future work

## 5.1 Conclusions

In this current study, we describe the ZnO/Pt nanoisland structure that was deposited on an Al<sub>2</sub>O<sub>3</sub> substrate to develop a highly stable high temperature hydrogen sensor and the corresponding result have been investigated. The influence of a high annealing temperature on physical and gas sensing performance of sputtered ZnO/Pt films have also been studied. Surface diffusion caused by the thermal annealing process produces a high surface to volume ratio based ZnO nanostructured NPs morphology with improved catalytic properties for the adsorption and desorption of hydrogen molecules at high temperatures (300°C). In comparison to the as-grown ZnO film, the annealed ZnO films have a higher intensity, a narrower FWHM of the (002) XRD peak, and better crystal content after RTA treatment. At 1000 ppm hydrogen gas exposure, a maximum reaction magnitude of 14.9 percent and a detection range of 100 to 1000 ppm for hydrogen gas were observed, with strong repeatability at 1000 ppm H<sub>2</sub> concentration. The substance has a smooth-textured reaction and a recovery time of 133/112 s for 1000 ppm at 300°C, as well as high hydrophobicity. At 1000 ppm hydrogen concentration, a robust sensing characteristic (~30 days), excellent stability against base resistance (~132.5Ω), and reaction (14.9%) were also achieved, as well as strong detection characteristics at 100 ppm hydrogen concentration. As a result, it was thought that our fabricated product could be a perfect candidate for H<sub>2</sub> detection in high-power industrial platforms.

## 5.2 Future work suggestions

Hydrogen detection over a large spectrum of greater stability, selectivity, and reaction time has a lot of study promise. The following is a list of possible issues of concern:

- Since hydrogen absorption is influenced by the connectivity and alloying between nanoscale catalytic metals, a higher surface to volume ratio dependent prototype underneath the metal can be built to improve the faster hydrogen absorption and desorption.
- Improving the substrate conductivity and creating a hierarchical nanostructured catalytic metal with a high surface to volume ratio will improve the extremely stable hydrogenation and dehydrogenation phenomena at higher operating conditions.
- Creating a heterogeneous interfacial structure with conductive materials like aluminum and zinc oxide (ZnO), as well as Pt, will speed up hydrogen molecule interaction.

### 5.3. List of publications by the author

#### First authorship

1. **Md Mayen Uddin**, Md Habibur Rahaman, Hyeon Cheol Kim, “**Highly stable hydrogen sensing properties of the ZnO/Pt nanoparticles layers deposited on alumina substrate for high temperature operated industrial applications**” “**Sensors and Actuators B: Chemical**” (7.460), under review.

#### Co-authorship

1. Md Habibur Rahaman, Usman Yaqoob, **Md Mayen Uddin**, Hyeon Cheol Kim, “**Highly catalytic hydrogen sensing properties of the nano percolated Pd/Mg/Ti nanoparticles layers decorated on Si substrate**” “**Applied Surface Science** (6.707)

#### Conference publications:

##### First authorship

1. **Md Mayen Uddin**, Md Habibur Rahaman, Hyeon Cheol Kim, “**High Temperature ZnO/Pt Nano Island Hydrogen Sensor**” “**IEIE**” “**ISSN 2005-0496**”
2. **Md Mayen Uddin**, Md Habibur Rahaman, Hyeon Cheol Kim, “**Highly Stable ZnO/Pt Nano Island Hydrogen Sensor for High Temperature**” “**IEIE**” “**ISSN 2005-0496**”



## REFERENCES

- [1] Y. Peng, J. Ye, L. Zheng, K. Zou, The hydrogen sensing properties of Pt–Pd/reduced graphene oxide based sensor under different operating conditions, *RSC Adv.* 6 (2016) 24880–24888.
- [2] Z. Chen, K. Hu, P. Yang, X. Fu, Z. Wang, S. Yang, J. Xiong, X. Zhang, Y. Hu, H. Gu, Hydrogen sensors based on Pt-decorated SnO<sub>2</sub> nanorods with fast and sensitive room-temperature sensing performance, *J. Alloys Compd.* 811 (2019) 152086.
- [3] Y.K. Gautam, A. Sanger, A. Kumar, R. Chandra, A room temperature hydrogen sensor based on Pd–Mg alloy and multilayers prepared by magnetron sputtering, *Int. J. Hydrog. Energy.* 40 (2015) 15549–15555.
- [4] A. Ghosh, C. Zhang, S.Q. Shi, H. Zhang, High-Temperature Gas Sensors for Harsh Environment Applications: A Review, *CLEAN – Soil Air Water.* 47 (2019) 1800491.
- [5] A. Hermawan, Y. Asakura, M. Kobayashi, M. Kakihana, S. Yin, High temperature hydrogen gas sensing property of GaN prepared from  $\alpha$ -GaOOH, *Sens. Actuators B Chem.* 276 (2018) 388–396.
- [6] M. Govindhan, B. Sidhureddy, A. Chen, High-Temperature Hydrogen Gas Sensor Based on Three-Dimensional Hierarchical-Nanostructured Nickel–Cobalt Oxide, *ACS Appl. Nano Mater.* 1 (2018) 6005–6014.
- [7] K. Mukherjee, S.B. Majumder, Hydrogen sensing characteristics of nano-crystalline Mg<sub>0.5</sub>Zn<sub>0.5</sub>Fe<sub>2</sub>O<sub>4</sub> thin film: Effect of film thickness and operating temperature, *Int. J. Hydrog. Energy.* 39 (2014) 1185–1191.
- [8] A. Ghosh, A. Maity, R. Banerjee, S.B. Majumder, Volatile organic compound sensing using copper oxide thin films: Addressing the cross sensitivity issue, *J. Alloys Compd.* 692 (2017) 108–118.

- [9] S. Mao, H. Zhou, S. Wu, J. Yang, Z. Li, X. Wei, X. Wang, Z. Wang, J. Li, High performance hydrogen sensor based on Pd/TiO<sub>2</sub> composite film, *Int. J. Hydrog. Energy*. 43 (2018) 22727–22732.
- [10] J. Lee, D.H. Kim, S.-H. Hong, J.Y. Jho, A hydrogen gas sensor employing vertically aligned TiO<sub>2</sub> nanotube arrays prepared by template-assisted method, *Sens. Actuators B Chem.* 160 (2011) 1494–1498.
- [11] J.H. Lee, S. Kwak, J.-H. Lee, I. Kim, Y.K. Yoo, T.H. Lee, Y.-S. Shim, J. Kim, K.H. Lee, Sputtered PdO Decorated TiO<sub>2</sub> Sensing Layer for a Hydrogen Gas Sensor, *J. Nanomater.* 2018 (2018) 1–8.
- [12] Y. Choi, M. Yang, S. Hong, H<sub>2</sub> sensing characteristics of highly textured Pd-doped SnO<sub>2</sub> thin films, *Sens. Actuators B Chem.* 134 (2008) 117–121.
- [13] M. Abinaya, R. Pal, M. Sridharan, Highly sensitive room temperature hydrogen sensor based on undoped SnO<sub>2</sub> thin films, *Solid State Sci.* 95 (2019) 105928.
- [14] I.H. Kadhim, H.A. Hassan, Q.N. Abdullah, Hydrogen Gas Sensor Based on Nanocrystalline SnO<sub>2</sub> Thin Film Grown on Bare Si Substrates, *Nano-Micro Lett.* 8 (2016) 20–28.
- [15] A. Nikfarjam, S. Fardindoost, A. Irajizad, Fabrication of Pd Doped WO<sub>3</sub> Nanofiber as Hydrogen Sensor, *Polymers*. 5 (2013) 45–55.
- [16] M.B. Rahmani, M.H. Yaacob, Y.M. Sabri, Hydrogen sensors based on 2D WO<sub>3</sub> nanosheets prepared by anodization, *Sens. Actuators B Chem.* 251 (2017) 57–64.
- [17] J.Z. Ou, M.H. Yaacob, J.L. Campbell, M. Breedon, K. Kalantar-zadeh, W. Wlodarski, H<sub>2</sub> sensing performance of optical fiber coated with nano-platelet WO<sub>3</sub> film, *Sens. Actuators B Chem.* 166–167 (2012) 1–6.
- [18] M. Yang, Y. Sun, D. Zhang, D. Jiang, Using Pd/WO<sub>3</sub> composite thin films as sensing materials for optical fiber hydrogen sensors, *Sens. Actuators B Chem.* 143 (2010) 750–753.

- [19] U.T. Nakate, R. Ahmad, P. Patil, Y. Wang, K.S. Bhat, T. Mahmoudi, Y.T. Yu, E. Suh, Y.-B. Hahn, Improved selectivity and low concentration hydrogen gas sensor application of Pd sensitized heterojunction n-ZnO/p-NiO nanostructures, *J. Alloys Compd.* 797 (2019) 456–464.
- [20] K.-S. Choi, S.-P. Chang, Effect of structure morphologies on hydrogen gas sensing by ZnO nanotubes, *Mater. Lett.* 230 (2018) 48–52.
- [21] V.S. Bhati, M. Hojamberdiev, M. Kumar, Enhanced sensing performance of ZnO nanostructures-based gas sensors: A review, *Energy Rep.* 6 (2020) 46–62.
- [22] H.S. Al-Salman, M.J. Abdullah, Fabrication and characterization of ZnO thin film for hydrogen gas sensing prepared by RF-magnetron sputtering, *Measurement.* 46 (2013) 1698–1703.
- [23] J.-H. Kim, A. Mirzaei, H.W. Kim, S.S. Kim, Pd functionalization on ZnO nanowires for enhanced sensitivity and selectivity to hydrogen gas, *Sens. Actuators B Chem.* 297 (2019) 126693.
- [24] K.J. Jeon, J.M. Lee, E. Lee, W. Lee, Individual Pd nanowire hydrogen sensors fabricated by electron-beam lithography, *Nanotechnology.* 20 (2009) 135502.
- [25] J. Eriksson, V. Khranovskyy, F. Söderlind, P.-O. Käll, R. Yakimova, A.L. Spetz, ZnO nanoparticles or ZnO films: A comparison of the gas sensing capabilities, *Sens. Actuators B Chem.* 137 (2009) 94–102.
- [26] P. Sundara Venkatesh, C.L. Dong, C.L. Chen, W.F. Pong, K. Asokan, K. Jeganathan, Local electronic structure of ZnO nanorods grown by radio frequency magnetron sputtering, *Mater. Lett.* 116 (2014) 206–208.
- [27] Y. Shi, M. Wang, C. Hong, Z. Yang, J. Deng, X. Song, L. Wang, J. Shao, H. Liu, Y. Ding, Multi-junction joints network self-assembled with converging ZnO nanowires as multi-barrier gas sensor, *Sens. Actuators B Chem.* 177 (2013) 1027–1034.

- [28] X.-M. Zhang, M.-Y. Lu, Y. Zhang, L.-J. Chen, Z.L. Wang, Fabrication of a High-Brightness Blue-Light-Emitting Diode Using a ZnO-Nanowire Array Grown on p-GaN Thin Film, *Adv. Mater.* 21 (2009) 2767–2770.
- [29] B. Xiang, P. Wang, X. Zhang, Shadi.A. Dayeh, D.P.R. Aplin, C. Soci, D. Yu, D. Wang, Rational Synthesis of p-Type Zinc Oxide Nanowire Arrays Using Simple Chemical Vapor Deposition, *Nano Lett.* 7 (2007) 323–328.
- [30] Y. Song, F. Chen, Y. Zhang, S. Zhang, F. Liu, P. Sun, X. Yan, G. Lu, Fabrication of highly sensitive and selective room-temperature nitrogen dioxide sensors based on the ZnO nanoflowers, *Sens. Actuators B Chem.* 287 (2019) 191–198.
- [31] Y.-S. Kim, W.-P. Tai, S.-J. Shu, Effect of preheating temperature on structural and optical properties of ZnO thin films by sol–gel process, *Thin Solid Films.* 491 (2005) 153–160.
- [32] Z.B. Fang, Z.J. Yan, Y.S. Tan, X.Q. Liu, Y.Y. Wang, Influence of post-annealing treatment on the structure properties of ZnO films, *Appl. Surf. Sci.* 241 (2005) 303–308.
- [33] S. Pittal, P.G. Snyder, N.J. Ianno, Ellipsometry study of non-uniform lateral growth of ZnO thin films, *Thin Solid Films.* 233 (1993) 286–288.
- [34] A. Rota, A. Martinez-Gil, G. Agnus, E. Moyon, T. Maroutian, B. Bartenlian, R. Mégy, M. Hanbücken, P. Beauvillain, Au island growth on a Si(111) vicinal surface, *Surf. Sci.* 600 (2006) 1207–1212.
- [35] A. Zdyb, The influence of annealing on the properties of ZnO:Al layers obtained by RF magnetron sputtering, (2018) 5.
- [36] Y.-C. Lee, S.-Y. Hu, W. Water, K.-K. Tiong, Z.-C. Feng, Y.-T. Chen, J.-C. Huang, J.-W. Lee, C.-C. Huang, J.-L. Shen, M.-H. Cheng, Rapid thermal annealing effects on the structural and optical properties of ZnO films deposited on Si substrates, *J. Lumin.* 129 (2009) 148–152.

- [37] H. Kumagai, Y. Sakamoto, H. Takeda, S. Matsunaga, M. Ohba, S. Inagaki, An Effective Synthetic Process for Pt-ZnO Composite and PtZn Alloy Using Spherical Coordination Polymer Particles as Precursors, *Chem. Lett.* 46 (2017) 1112–1115.
- [38] D. Jung, M. Han, G.S. Lee, Fast-Response Room Temperature Hydrogen Gas Sensors Using Platinum-Coated Spin-Capable Carbon Nanotubes, *ACS Appl. Mater. Interfaces.* 7 (2015) 3050–3057.
- [39] M. Rahaman, U. Yaqoob, H. Kim, Fast Hydrogenation and Dehydrogenation of Pt/Pd Bimetal Decorated over Nano-Structured Ag Islands Grown on Alumina Substrates, *Sensors.* 19 (2018) 86.
- [40] A. Kozbial, Z. Li, C. Conaway, R. McGinley, S. Dhingra, V. Vahdat, F. Zhou, B. D'Urso, H. Liu, L. Li, Study on the Surface Energy of Graphene by Contact Angle Measurements, *Langmuir.* 30 (2014) 8598–8606.
- [41] P. Blumentrit, M. Yoshitake, S. Nemšák, T. Kim, T. Nagata, XPS and UPS study on band alignment at Pt–Zn-terminated ZnO(0001) interface, *Appl. Surf. Sci.* 258 (2011) 780–785.
- [42] J. Liu, L. Zhang, J. Fan, B. Zhu, J. Yu, Triethylamine gas sensor based on Pt-functionalized hierarchical ZnO microspheres, *Sens. Actuators B Chem.* 331 (2021) 129425.
- [43] J. Low, B. Dai, T. Tong, C. Jiang, J. Yu, In Situ Irradiated X-Ray Photoelectron Spectroscopy Investigation on a Direct Z-Scheme TiO<sub>2</sub>/CdS Composite Film Photocatalyst, *Adv. Mater.* 31 (2019) 1802981.
- [44] M.H. Rahaman, U. Yaqoob, H.C. Kim, Fast hydrogenation and dehydrogenation of Pd-Mg bimetal capped Ti nanoparticles layer deposited on Si substrate, *Sens. Actuators B Chem.* 309 (2020) 127814.
- [45] I.-D. Kim, A. Rothschild, H.L. Tuller, Advances and new directions in gas-sensing devices, *Acta Mater.* 61 (2013) 974–1000.

- [46] Z. Yuan, Z. Feng, L. Kong, J. Zhan, X. Ma, Simple synthesis of porous ZnO nanoplates hyper-doped with low concentration of Pt for efficient acetone sensing, *J. Alloys Compd.* 865 (2021) 158890.
- [47] I. Paseka, Electrochemical titration of hydrogen adsorbed on supported platinum catalysts, *Appl. Catal. Gen.* 329 (2007) 161–163.
- [48] M.H. Rahaman, U. Yaqoob, M.M. Uddin, H.C. Kim, Highly catalytic hydrogen sensing properties of the nano percolated Pd/Mg/Ti nanoparticles layers decorated on Si substrate, *Appl. Surf. Sci.* 549 (2021) 149203.
- [49] Q.A. Drmosh, Z.H. Yamani, A.H. Hendi, M.A. Gondal, R.A. Moqbel, T.A. Saleh, M.Y. Khan, A novel approach to fabricating a ternary rGO/ZnO/Pt system for high-performance hydrogen sensor at low operating temperatures, *Appl. Surf. Sci.* 464 (2019) 616–626.
- [50] Y. Sun, H.H. Wang, High-Performance, Flexible Hydrogen Sensors That Use Carbon Nanotubes Decorated with Palladium Nanoparticles, *Adv. Mater.* 19 (2007) 2818–2823.

## **APPENDIX – CHARACTERIZATION**

### **A.1 Evaluation methods for materials characterization**

3D atomic force microscopy (AFM, MultiMode V) was utilized to examine the roughness and RMS grain size of nanostructured ZnO nanoparticles. Cold field emission scanning electron microscopy (Cold FE-SEM, SU8220) was utilized to study the surface morphology of ZnO/Pt nanoparticles on an alumina substrate under various annealing conditions. A high-resolution X-ray diffraction (XRD, D/MAX2500V/PC, Ulsan, Korea) with Cu K $\alpha$  ( $\lambda = 0.154$  nm) radiation over a two-dimensional screening spectrum of 10–90° was used to examine crystallite size and material composition of the nanoparticles. X-ray photoelectron spectroscopy (XPS, Thermo Fisher K-Alpha) was used to verify the elemental composition, with Al K $\alpha$  radiation as a medium of X-rays. Energy dispersive X-ray spectroscopy (EDS, JEOL, JEM-2100 F) was used to examine the textural properties of the as-prepared samples. Goniometry of contact angles (Kruss DSA 100 drop form analyzer, Ulsan, Korea) was used to calculate water droplet contact angles using the sessile drop technique at room temperature. A micro-syringe was used to drop deionized water droplets (approximately 5  $\mu$ L) on the thin film surfaces.

### **A.2 Evaluation methods for sensing measurement hydrogenation and dehydrogenation measurement:**

The as-fabricated devices were measured in a chamber at a fixed temperature of 300°C against different H<sub>2</sub> concentrations to determine smooth response/recovery and stability properties. For all measurements and data processing, a Keithley probe station (SCS-4200) was used with a specified switching voltage of 1V, and a configurable heater installed with the device holder in the gas chamber. To control the concentration

of hydrogen gas in synthetic atmosphere, an automated flow rate monitoring system (GMC 1200, ATOVAC, Ulsan, Korea) was used. At a steady state rate of 200 sccm, different gases with various H<sub>2</sub> volumes were supplied to the chamber. Between every H<sub>2</sub> pulse, synthetic gas was delivered to the gas chamber to allow the system surface to adapt with atmospheric conditions. The following equation was used to regulate and quantify the gas concentration:

$$\text{Desired gas}_{\text{con.}} (\text{ppm}) = \frac{\text{Flowrate}_{\text{gas}}}{\text{Flowrate}_{\text{gas}} + \text{Flowrate}_{\text{syntheticair}}} \times \text{Supplied gas}_{\text{con.}} (\text{ppm}) \quad (1)$$

The sensor response magnitude was defined as:

$$S, (\%) = \frac{G_g - G_a}{G_a} \times 100 \quad (2)$$

where  $G_g$  and  $G_a$  are the sensor's conductance of H<sub>2</sub> gas and air stimulation at different ppm, respectively. The time it took to hit 90% of the overall conductance transition and the time it took for the conductance to return to its original value were used to calculate the reaction and recovery time of the as-prepared sensor.